Cross-Frequency Coupling as a Neural Substrate for Prediction Error Evaluation: A Laminar Neural Mass Modeling Approach

NE TN0384 (v2, March 1 2025)

Giulio Ruffini*[1], Edmundo Lopez-Sola*[1,2], Raul Palma[2], Roser Sanchez-Todo[1,2], Jakub Vohryzek[2], Francesca Castaldo[1], and Karl Friston[3]

[1]Neuroelectrics, Barcelona, Spain
[2]Universitat Pompeu Fabra, Barcelona, Spain
[3]Wellcome Centre for Human Neuroimaging, University College London, London, UK

March 19, 2025

Abstract

Predictive coding frameworks suggest that neural computations rely on hierarchical error minimization, where sensory signals are evaluated against internal model predictions. However, the neural implementation of this inference process remains unclear. We propose that cross-frequency coupling (CFC) furnishes a fundamental mechanism for this form of inference. We first demonstrate that our previously described laminar neural mass model (LaNMM) supports two key forms of CFC: (i) Signal-Envelope Coupling (SEC), where low-frequency rhythms modulate the amplitude envelope of higher-frequency oscillations, and (ii) Envelope-Envelope Coupling (EEC), where the envelopes of slower oscillations modulate the envelopes of higher-frequency rhythms. Then, we propose that—by encoding information in signals and their envelopes—these processes instantiate a hierarchical "Comparator" mechanism at the columnar level. Specifically, SEC generates fast prediction-error signals by subtracting top-down predictions from bottom-up oscillatory envelopes, while EEC operates at slower timescales to instantiate gating—a critical computational mechanism for precision-weighting and selective information routing. To establish the face validity—and clinical implications of—this proposal, we model perturbations of these CFC mechanisms to investigate their roles in pathophysiological and altered neuronal function. We illustrate how, in disorders such as Alzheimer's disease, disruptions in gamma oscillations following dysfunction in fast-spiking inhibitory interneurons impact Comparator function with an aberrant amplification of prediction errors in the early stages and a drastic attenuation in late phases of the disease. In contrast, by increasing excitatory gain, serotonergic psychedelics diminish the modulatory effect of predictions, resulting in a failure to attenuate prediction error signals (c.f., a failure of sensory attenuation). Together, these results establish cross-frequency coupling—across temporal scales—as candidate computational processes underlying hierarchical predictive coding in health and disease.

*co-First author; Email: giulio.ruffini@neuroelectrics.com, edmundo.lopez@neuroelectrics.com

Contents

1 Introduction **4**
1.1 Background and Motivation 4
1.2 The Role of Oscillations 6
1.3 The Laminar Neural Mass model (LaNMM) 7
1.4 Amplitude Modulation for Information Encoding and Processing 10

2 Methods **11**
2.1 Dynamics and Cross-Frequency Coupling in the LaNMM 13
2.2 Comparator I: Implementation Using SEC 15
2.3 Comparator II: The role of EEC for precision weighting 17
2.4 Disruption of Comparator Function 18

3 Results **19**
3.1 The LaNMM Sustains Robust SEC and EEC for a Wide Range of Mean Inputs . 19
3.2 SEC subserves Fast-Time Comparator Function 21
3.3 EEC subserves Slow-Time Precision Modulation 21
3.4 Psychedelics and Interneuron Pathology Disrupt the Comparator 21

4 Discussion **26**
4.1 Interpretation of results 26
4.2 Predictive coding and precision 27
4.3 Gating by Inhibition and Predictive Routing 28
4.4 Error Evaluation Dysfunctions 30
4.5 Previous Computational Models of CFC and Prediction Error 34
4.6 Limitations 35

5 Conclusion **36**

Appendix **51**

Highlights

- Using an encoding scheme where information is encoded in signals, their envelopes, and envelopes of envelopes, we show how to implement prediction error and precision modulation in a neural mass model through cross-frequency coupling (CFC).
- We use the laminar neural mass model (LaNMM), which integrates Jansen-Rit and pyramidal interneuron gamma (PING) submodels to display fast and slow rhythms and provides mechanisms for a) *Signal-Envelope Coupling (SEC)*, where slow-wave activity modulates the amplitude envelope of fast oscillations (analogous to phase-amplitude coupling), and b) *Envelope-Envelope Coupling (EEC)*, where the envelopes of slower oscillations modulate the envelopes of higher-frequency rhythms.
- We show how to use the LaNMM to implement information-based prediction-error evaluation (as used in Active Inference and Kolmogorov Theory), computing the approximate precision-weighted difference between incoming sensory data (envelopes) to internal model predictions (signals or envelopes).
- We show that using these mechanisms, the Comparator mechanism can operate at multiple levels and timescales, generating fast prediction-error signals (via SEC) and slower gating signals that encode context (e.g., precision) (via EEC).
- The model provides insights into the cognitive consequences of LaNMM alterations in the context of predictive coding. First, we study disorders of fast-spiking interneurons, such as Alzheimer's Disease (AD). In the early stages of AD (mild PV+ impairment), error evaluation and precision are disrupted (inflated error and reduced gating/weight of predictions), leading to higher prediction errors even when signals match. In later stages (high PV+ impairment), prediction errors are suppressed regardless of predictions or their precision. Serotonergic psychedelics increase the effective weight of inputs and diminish that of predictions, resulting in higher prediction error signals.

1 Introduction

1.1 Background and Motivation

Predictive coding has become a central framework for understanding cognitive processing. It holds that the brain continuously generates predictions about incoming sensory data and updates these predictions in response to mismatches or prediction errors.[1,2]

Prediction errors are thought to be passed forward through cortical hierarchies to update higher-level beliefs, while predictions are sent via feedback connections to explain away expected input.[3,4] Notably, this bidirectional information flow is reflected in the nature of the extracellular signal—its fundamental features remain consistent across spatial and temporal scales, from microelectrode recordings to large-scale scalp measurements.[5] This scale-invariance implies that the same principles underwrite local and global dynamics, a property that may facilitate the orchestration of predictive processes under deep (i.e., hierarchical) world models. Neural oscillations are hypothesized to play a key role in this hierarchical inference: higher-frequency activity (particularly in the gamma band, ∼30–100 Hz) is often associated with feedforward signaling of surprise or prediction error, whereas lower-frequency rhythms (alpha/beta bands, ∼8–30 Hz) are linked to top-down predictive signals.[3,4] Cross-frequency coupling (CFC), such as the phase or amplitude of slower waves modulating the amplitude of faster oscillations, is thought to coordinate communication between levels of the hierarchy.[6] This contextual coordination is sometimes cast in terms of minimizing precision-weighted prediction errors where precision (i.e., estimated signal-to-noise in prediction errors, see Appendix D) is encoded in the excitability of neuronal populations encoding prediction errors: c.f., Precision and Kalman gain in Bayesian filtering formulations of predictive coding.[1,7,8] The empirical support for this scheme comes from studies showing that unpredictable stimuli (violating expectations) evoke increased gamma-band power and spiking that propagate feedforward, while predictable contexts enhance alpha/beta oscillations and connectivity in deep cortical layers, which can suppress gamma drive.[3,4]

In Active Inference theory (AIF), predictive coding provides a computational foundation for how the brain continuously minimizes variational free energy through a hierarchical interplay of top-down predictions (priors) and bottom-up prediction errors (data)—evaluating prediction errors (perception), updating its model state and acting on the environment to fulfill these predictions (action).[9,10] Kolmogorov Theory (KT) formalizes this framework through Algorithmic Information Theory (AIT), where algorithmic *agents* optimize predictions by finding short (compressive) models of the world to optimize an Objective function. In the Bayesian framework of AIF, to achieve this, agents optimize the marginal likelihood of sensory input under a generative (i.e., compressive world) model of that input, where the log marginal likelihood or log evidence is bounded by variational free energy. Under the assumptions of predictive coding (i.e., continuous latent states and well-behaved random fluctuations), the objective function in AIF reduces to a mixture of precision-weighted prediction errors.[9,10] In KT, the Objective function represents the homeostatic and the tele-homeostatic (reproduction) goals of the agent, which indirectly translate into goals on minimizing prediction error[11–17]—see Figure 1. In both

cases, measuring and managing prediction error is necessary.

Although the predictive biological brain operates as a putative analog computational system, seemingly removed from the algorithmic digital agents described in KT, these paradigms are closely related. Both analog (e.g., brains) and digital algorithmic agents aim to model and track the world, a process that fundamentally relies on computing sensory prediction errors to update internal representations (information theory deals with both discrete and continuous notions of information under the same umbrella[18]). Predictive coding requires a *Comparator* mechanism to evaluate prediction error ($\mathcal{E}$) to quantify how predictions $\mathcal{P}$ diverge from sensory input $\mathcal{I}$ to update predictions (see Figure 1). The Comparator assesses discrepancies, driving model adjustments to reduce $\mathcal{E}$ and aligning sensory and generative model dynamics. From a Bayesian filtering perspective, this can be read as Bayesian belief updating.[2,19]

In this paper, we start by defining an information *encoding* framework inspired by amplitude modulation (AM) radio to explore, through neural mass modeling, the mechanisms by which prediction errors can be evaluated, identifying neural substrates and oscillatory instantiations of the Comparator function at the mesoscopic scale.

Our definition of the Comparator highlights essential distinctions between generating prediction errors and other important processes such as inhibition, gating,[20] and routing,[21] which can be read as predicting and instantiating the precision required to minimize precision-weighted prediction errors. In this setting, precision corresponds to an encoding of confidence, which plays a key role in weighting prediction errors that compete for belief updating. In Bayesian filtering schemes, this would correspond to optimizing the Kalman gain.[10] In Psychology, this aspect of predictive coding has been associated with selective attention, attentional gain, and sensory attenuation. Physiologically, this context-sensitive aspect of predictive coding is usually attributed to cortical gain control or excitation-inhibition balance. The link between attention and physiological encoding of precision or uncertainty is nicely illustrated by the notion of communication through coherence.[3,22–26]

In the binary encoding context, the Comparator is represented logically by the "exclusive" OR operation (XOR). XOR returns one if the inputs are different and zero otherwise, which can be expressed as $\mathcal{E} \sim \mathrm{XOR}(\mathcal{I}, \mathcal{P}) = \mathcal{I} \oplus \mathcal{P} = (\mathcal{I} \wedge \neg\mathcal{P}) \ \vee \ (\neg\mathcal{P} \wedge \mathcal{I})$, where $\mathcal{E}$ represents the prediction error, $\mathcal{I}$ the input and $\mathcal{P}$ the prediction. In predictive coding, the Comparator produces precision-weighted prediction errors that are crucial for model updating, directly informing adjustments to the generative model. Similarly, prediction errors are actively employed in Kalman filtering,[27] enabling continuous updates to model parameters based on incoming sensory information.[19] Thus, in the analog version, which is more appropriate for the physiological context, we generalize the Comparator function to evaluate the *weighted* difference between data and model, i.e.,

$$\mathcal{E}(t) \sim \Pi \cdot \big(\mathcal{I}(t) - \mathcal{P}(t)\big) \tag{1}$$

or some approximation to this quantity. Here, Π refers to the *Precision* (in reference to the Kalman filtering, see Appendix D) assigned to the prediction error, which we can think of as a multiplicative factor (or, more generally, an operator). Precision modulates the impact of the

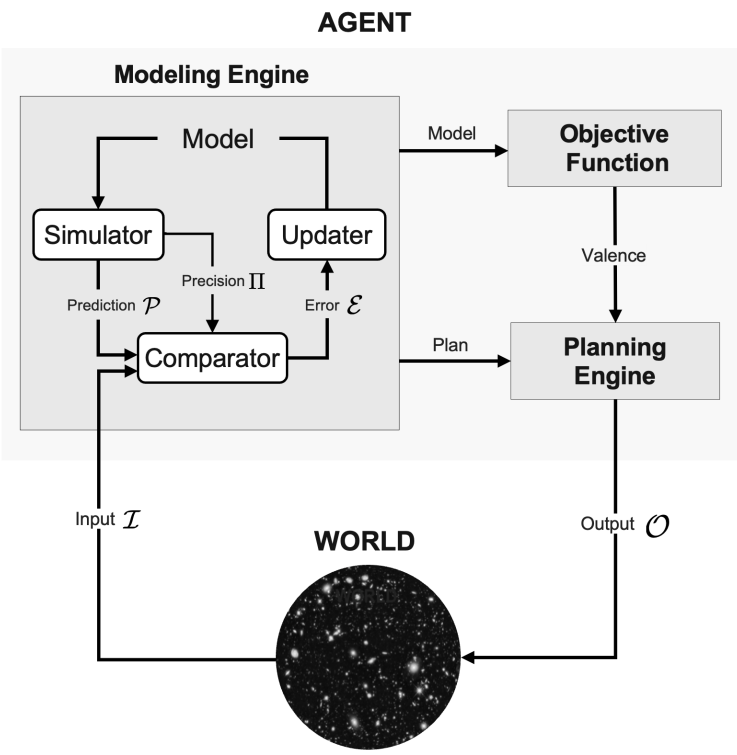

Figure 1: The Comparator in KT algorithmic agents. An algorithmic agent is an information-processing system with an Objective Function that interacts bidirectionally with the external world, creating and running compressive models, planning, and acting to maximize its Objective Function.[14–16] The agent interacts dynamically with its environment, continuously exchanging data inputs ($\mathcal{I}$) and outputs ($\mathcal{O}$). The *Modeling Engine* formulates predictions ($\mathcal{P}$) and the estimated precision (Π) of the prediction error to evaluate the precision-weighted prediction error ($\mathcal{E}$) in the Comparator to update the Model. The *Comparator* is a key agent element monitoring the performance of the modeling engine and providing the information for model updates.

discrepancy of model and data for model updates (loosely, the higher the precision, the greater the model update). More precisely, precision specifically refers to the inverse covariance of the prediction errors. However, in what follows, we will use the term somewhat loosely here to refer to inverse covariance (confidence) associated with a given signal (input, prediction, error).

1.2 The Role of Oscillations

There is a natural gradation from neuronal spiking to fast oscillations (gamma band), to slower rhythms such as beta, alpha, theta and delta.[28,29] These rhythms also exhibit distinct spatial coherence scales. Gamma oscillations tend to synchronize within local neuronal assemblies, whereas slower rhythms (e.g., theta, alpha) can coordinate across larger cortical networks.[28] Consequently, information is encoded and integrated across these distinct spatiotemporal scales. Gamma oscillations (30–100 Hz) are critical for integrating information, feature binding, and encoding task-relevant signals across cortical circuits.[25,28,30] In motor cortex, gamma supports movement control and learning,[31] while in the hippocampus it aids episodic memory formation.[32] Disruptions in gamma are linked to neuropsychiatric disorders,[33,34] and

gamma entrainment via sensory stimulation shows therapeutic promise.[35,36] Gamma synchronization—enabling communication through coherence—facilitates selective routing and feature binding.[25,30,37]

Animal studies further indicate that unpredicted stimuli evoke robust gamma (and theta) responses in superficial cortical layers, consistent with the feedforward transmission of prediction errors.[38] Collectively, gamma rhythms are fundamental carriers of information for perception, attention, memory, and behavior.[39] In contrast, alpha (8–12 Hz) and theta (4–8 Hz) oscillations are associated with inhibition, attentional gating, and cognitive control.[20,40–44] While gamma typically propagates feedforward, alpha is implicated in feedback processing.[45] Moreover, alpha and beta oscillations have been shown to encode stimulus predictions and modulate spatial attention by selectively amplifying relevant signals.[46–49]

An important example of CFC,[6] Phase-amplitude coupling (PAC) between gamma and slower brain rhythms (theta, alpha, spindle, slow, and ultra-slow) is well documented.[28,50] For example, theta oscillations organize gamma activity via PAC, with the theta phase modulating the gamma envelope to segment complex information (e.g., speech into syllabic units).[51–53] Electroenchephalography (EEG), Magnetoencephalography (MEG), and Electrocorticography (ECoG) studies confirm that low-frequency responses track the temporal envelope of attended speech, while high-gamma envelopes selectively encode auditory information.[54–58] Together, CFC among gamma, alpha, and theta rhythms establish a dynamic balance between local processing and contextual coordination, which are hypothesized to subserve efficient and flexible neural computation.[59,60]

Supporting this idea, abnormal PAC has been observed in several neurological and psychiatric disorders. In Parkinson's disease, increased beta–gamma PAC in the motor cortex correlates with symptom severity and responds to medication,[61–63] with significant changes emerging in advanced stages.[64] Similarly, in AD, PAC (theta/alpha to gamma) is decreased relative to healthy controls and correlates with cognitive impairment.[65–67] Region-specific reductions in PAC, such as in the lower left temporoparietal area[68] and in the hippocampus and medial prefrontal cortex of transgenic AD models,[69] are likely driven by amyloid-beta and tau pathologies, with reduced gamma PAC also reported in the left parahippocampal cortex.[67] Gamma entrainment via sensory[70,71] or electrical stimulation[72]—which appears to modulate theta–gamma PAC in the frontal cortex[73]—has been proposed as a potential treatment for AD. PAC disruptions are also evident in psychiatric conditions.[74,75,75,76] Finally, psilocybin has also been shown to disrupt PAC (theta–gamma) in a dose-dependent manner in animal models.[77]

1.3 The Laminar Neural Mass model (LaNMM)

Cortical function emerges from dynamics on cortical and subcortical hierarchies with multiscale architectural features.[78,79] These networks can be modeled using *connectomes*[80] and node activity generated by physiologically realistic mesoscopic neural mass models (NMMs)[81] to provide a high-level representation of the mean activity of large neuronal populations. A typical cortical column in the mammalian neocortex is estimated to contain on the order of 10^4 neurons, with some regions or species exhibiting counts closer to 10^5 neurons.[82] For instance, in primary

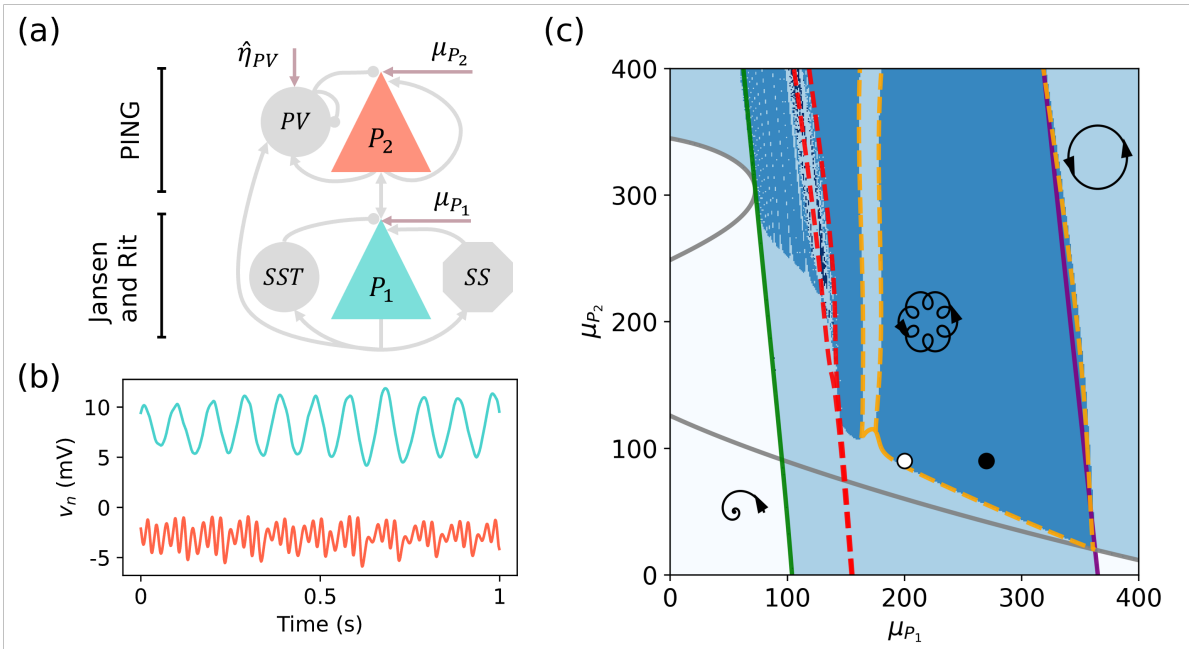

Figure 2: Laminar Neural Mass Model Overview. (a) Laminar neural mass model architecture. Driving inputs studied in the model (all glutamatergic) are displayed (μ_{P_1} is the mean input parameter to P_1, μ_{P2} is the mean input parameter to P_2, as well as stochastic zero mean input to PV). (b) Sample signals. (c) Two-parameter bifurcation diagram of the LaNMM model as a function of the external inputs μ_{P_1} and μ_{P_2} obtained using the continuation software AUTO-07p.[85] Symbols indicate the dynamical regimes within the colored regions: steady-state (white), periodic (light blue), and quasi-periodic (dark blue). The lines represent bifurcations, as described in the main text. The white dot marks the mean input parameter values used in Sanchez-Todo et al. (2023),[86] $(\mu_{P_1}, \mu_{P_2}) = (200, 90)$ Hz. The black dot indicates the representative values chosen in this study, $(\mu_{P_1}, \mu_{P_2}) = (270, 90)$ Hz, which place the model deeper into the quasi-periodic regime and display a stronger EEC (see Figures 4 and H1).

sensory cortices—such as the visual or somatosensory areas—a column is often characterized by roughly 10,000 neurons, although precise numbers can vary based on anatomical definitions and the specific cortical region. This mesoscopic scale—situated between single neurons and large-scale networks—provides a natural level of description for many electrophysiological phenomena. NMMs are designed to capture the aggregate dynamics of large neuronal populations by averaging individual activity into mean-field variables, such as average membrane potentials or firing rates.[83,84] Given that a cortical column comprises tens of thousands of neurons, the underlying assumption that microscopic fluctuations average out is largely justified. This averaging allows NMMs to reproduce key oscillatory and coupling phenomena, including cross-frequency interactions and the propagation of prediction errors, without modeling each neuron individually. Thus, NMMs are well-suited to describe mesoscopic dynamics within cortical columns, although they necessarily abstract away finer-scale micro-circuital details.

We have previously introduced a *laminar* neural mass model (LaNMM)[86,87] optimized from laminar recordings from the macaque prefrontal cortex[88] and designed to capture both superficial-layer fast and deeper-layer slow oscillations along with their interactions (cross-frequency coupling), such as PAC and amplitude-amplitude anti-correlation (AAC). The spectrolaminar motif

is ubiquitous across the primate cortex.[89] The LaNMM combines conduction physics with two NMMs—Jansen-Rit and Pyramidal Interneuronal Network Gamma (PING) subpopulations at slow and fast frequencies, respectively—to simulate depth-resolved electrophysiology.

Although the LaNMM is only one of several potential modeling frameworks, it provides a powerful and physiologically realistic tool to address the broader hypothesis that (1) information can be encoded both in ongoing signals and in their amplitude envelopes, and (2) prediction-error evaluation may be instantiated by cross-frequency coupling in cortical columns—particularly signal-to-envelope and envelope-to-envelope couplings. As we show, the LaNMM allows for a dynamic instantiation of the Comparator, facilitating the analysis of how prediction errors and top-down predictions may be integrated across different cortical lamina. By analyzing cross-frequency coupling in the model simulations, one can gain insight into how fast and slow oscillatory interactions may underpin prediction error generation, routing, and inhibition in hierarchical cortical processing.

The LaNMM is a biologically plausible extension of existing neural mass models (NMMs), integrating realistic cortical architectures with self-sustaining oscillatory dynamics and emergent cross-frequency coupling (CFC). This design makes it well-suited for investigating cortical processing and oscillatory interactions. By featuring two interacting populations—each capable of autonomously generating oscillations—the LaNMM provides a physiologically grounded framework for studying cortical rhythms. In contrast, other models such as PING,[29] Jansen–Rit (JR),[83] Wendling,[90] and Chehelcheraghi[91,92] differ in their structural assumptions and how they produce oscillations or cross-frequency coupling. Notably, the LaNMM does not rely on stochastic inputs to sustain its rhythms. For example, the Chehelcheraghi models require noise to induce inhibition-based gamma (ING) and CFC, whereas the LaNMM combines JR and PING sub-models, each generating slow or fast rhythms independently—leading naturally to phase-amplitude (PAC) and amplitude-amplitude coupling (AAC).

Furthermore, the LaNMM is explicitly designed with a cortical laminar architecture amenable for realistic physical measurements,[86,93,94] distinguishing it from the lumped population models of PING, JR, and Wendling. While the PING model primarily produces gamma oscillations through an excitatory-inhibitory loop and the JR/Wendling models focus on alpha rhythms with additional fast inhibitory loops, the LaNMM naturally produces multiple frequency bands by leveraging laminar interactions. This makes it particularly suited for modeling observed laminar-specific oscillations, such as deep-layer alpha/beta modulating superficial-layer gamma, as seen in frontal and parietal cortices.[23] Additionally, the model's structure allows generalization beyond the alpha-gamma framework, accommodating different slow-fast frequency pairs (e.g., theta-beta, theta-gamma, beta-gamma) through parameter adjustments. This flexibility further enhances its relevance for modeling diverse cortical dynamics across brain regions (some examples are given in Appendix F).

Finally, the LaNMM fits squarely in the context of hierarchical processing and predictive coding. There exist evident asymmetries in hierarchical cortical connectivity, particularly in the distinct roles of feedforward and feedback pathways in sensory processing.[95,96] Anatomical studies have established that feedforward pathways typically originate from superficial layers

and project to granular layers, while feedback pathways arise from deeper layers, connecting to non-granular areas, supporting a hierarchical processing model. Functionally, feedforward and feedback connections also differ in frequency domains. Feedforward signals often use gamma-band frequencies and are associated with prediction error transmission, while feedback signals utilize lower alpha and beta frequencies, hypothesized to convey predictions and in alignment with predictive coding models.[95] In this framework, feedforward connections deliver prediction errors to higher-order areas, while feedback signals transmit top-down predictions to explain sensory input. Experimental studies support this model, showing that gamma coherence is stronger in feedforward pathways, while alpha/beta coherence is more prominent in feedback pathways, suggesting a mechanism where faster frequencies convey discrepancies and slower frequencies signal model-driven predictions.[95]

1.4 Amplitude Modulation for Information Encoding and Processing

In digital communication systems, information is typically represented as a sequence of binary digits. In contrast, analog systems and biological networks convey information via continuous signals. A classic example is AM radio, where a high-frequency carrier wave is modulated by a low-frequency signal so that the carrier's amplitude (its envelope) encodes the desired information. Neural systems appear to operate on a similar principle, encoding information in aspects such as signal power, phase, or envelope.[97] For instance, high gamma-band activity in the auditory cortex exhibits amplitude modulation that closely tracks the stimulus envelope,[98] and Pasley et al. (2012)[99] demonstrated that speech could be reconstructed from the high gamma power envelope extracted from ECoG recordings.

In our framework for error evaluation, and as further discussed in Ruffini et al. (2025),[100] we assume that oscillatory information is encoded in the slow (top-down) *signal*, its *envelope*, or in the fast signal's *envelope*. As the dynamic impact of error signals is proportional to their power, "loud" (i.e., precise) signals exert a stronger effect on predictive processing (i.e., belief updating in higher hierarchical levels). In this view, the Comparator mechanism at each hierarchical level does not operate on the full detail of the gamma signal but rather on a coarse-grained version—the amplitude envelope—that approximates the difference between internal predictions and incoming sensory data. A successful match yields a lower power gamma signal with a reduced modulation index, whereas a discrepancy results in a modulated signal conveying the prediction error.

AM radio provides a relevant analogy. It transmits information—such as speech or music—by encoding it as variations in the dynamic amplitude (envelope) of a high-frequency carrier wave. In more detail, the fast carrier signal, expressed as $C(t) = A_c \cos(2\pi f_c t)$, is modulated by a slower base-band (information) signal $m(t)$ to produce $S(t) = A_c\,[1 + a\,m(t)]\cos(2\pi f_c t)$, where $a < 1$ is the *modulation index* ensuring the envelope reliably follows $m(t)$. At the receiver, demodulation extracts the original information from the envelope variations of $S(t)$. In the Hierarchical Amplitude Modulation (HAM) model discussed elsewhere,[100] information is similarly encoded not only in the raw oscillatory signals but also in their successively extracted envelopes, establishing a multiscale coding scheme that reflects the brain's hierarchical organization—and

implicit depth of its generative world model. In this context, information is encoded in the signals or their envelopes, and we will focus on their couplings. For this reason, rather than PAC, we will focus on signal-to-envelope coupling.

In the following sections, we detail how our model capitalizes on the above encoding mechanisms. First, we show that the LaNMM provides concrete mechanisms for SEC and EEC. In SEC, slow-wave activity modulates the amplitude envelope of fast oscillations (analogous to phase-amplitude coupling), while in EEC, slower envelopes modulate amplitude-amplitude interactions, thereby adding an extra layer or order of predictive control. In brief, we implicitly associate (fast) phase amplitude coupling with the encoding of first-order content of prediction errors, while the (slow) amplitude-amplitude coupling is associated with the encoding of second-order context in which content is inferred, where the context can be regarded as the precision (i.e., inverse variance) or second-order statistics of first-order prediction errors.[8,101]

Next, we demonstrate how the LaNMM can provide weighted prediction-error evaluation, i.e., computing an approximate difference between incoming sensory data (as captured in input signal envelopes) and internal model predictions (either as signals or their envelopes). These mechanisms enable the Comparator to operate across multiple levels and timescales—generating fast prediction-error signals via SEC and slower context-sensitive weighted gating signals via EEC.

To explore how alterations in the LaNMM and prediction error function can shed light on the adverse effects observed in certain pathological or altered states, we discuss how deficits in fast inhibitory synapses, as seen in Alzheimer's Disease, and increased glutamate receptor gain, characteristic of serotonergic psychedelic states, may disrupt the Comparator process and compromise effective information processing.

Finally, although the analysis will center on the LaNMM as originally described,[86,102] it can be extended to other LaNMM parameterizations and frequency schemes (not necessarily alpha and gamma at 40 Hz), or indeed other computational models displaying CFC (positive SEC and negative EEC).

2 Methods

Figure 3 provides an overview of the Comparator mechanism in predictive coding, which we will implement in our LaNMM. Here, incoming "input" $\mathcal{I}$ is combined with a "prediction" $\mathcal{P}$, producing a precision-weighted "error" signal $\mathcal{E}$ propagating up the hierarchy.

Information is encoded in the "fast envelope" of the input signal $\mathcal{I}$ and in the prediction signal $\mathcal{P}$ itself, while input precision (gain) is encoded in the slow envelope of the input (envelope of the envelope, i.e., average power) and prediction precision in the envelope of the prediction signal. More specifically, the envelope of the prediction signal encodes the inverse precision of the prediction $\Pi_{\mathcal{P}}^{-1}$ (i.e., covariance or uncertainty), while the envelopes of input and error encode their precision, $\Pi_{\mathcal{I}}$, and $\Pi_{\mathcal{E}}$ respectively (inverse covariance or confidence).

In line with predictive coding frameworks, we aim to show how the LaNMM can explicitly

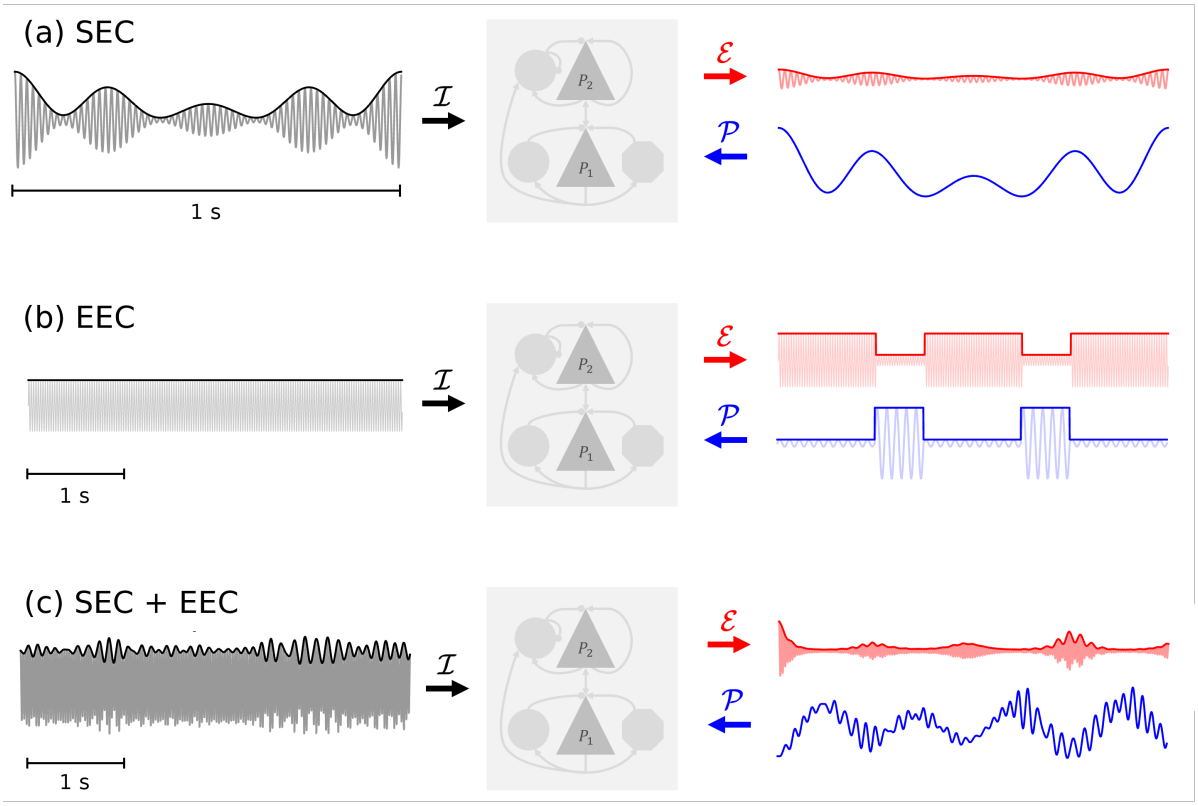

Figure 3: Laminar model concept implementation of the evaluation of prediction error ($\mathcal{E}$) via two timescales and two mechanisms: a) Signal-Envelope coupling (SEC) mediated evaluation of prediction error, where the incoming information is encoded in the (fast) envelope of the carrier, and the prediction is directly the slower signal; b) Envelope-Envelope coupling (EEC) implementation of precision computation (digital simplification), where the precision of prediction errors is modulated by the envelope of the slower signal flowing downstream. Panel (c) illustrates the combination of both mechanisms, where precision (very slow envelope) and predictions (signals) are encoded into the same signal ($\mathcal{P}$). The LaNMM (center) includes two bidirectionally interacting subpopulations.[86] Bottom-up input data ($\mathcal{I}$) arrives at the PING subpopulation pyramidal cell P_2 encoded in the fast oscillation envelope, while top-down weighted predictions ($\mathcal{P}$) arrive encoded in slower signals (alpha band in the model) at the bottom JR population pyramidal cell P_2 or at the PV cell in the PING subpopulation. The interaction alters the dynamics of P_2, which produces an approximate, weighted difference of input and prediction $\mathcal{E}$ encoded in the envelope.

encode how mismatch signals (errors) update and refine internal predictions, thereby emulating a biologically plausible Comparator process at multiple cortical levels. In this paper, we will focus on local processing at a single column and the implementation of modulation, demodulation, and Comparator mechanisms. The analysis of coupled columns for a full implementation of predictive coding will be pursued elsewhere.

For the implementation of the Comparator, we rely on oscillations and their cross-frequency coupling properties. In our demonstration, we focus on a particular combination of inputs. However, the mean inputs of the LaNMM nodes in a whole brain model will vary as a function of their connectivity to other nodes. To illustrate the range of applicability of the model, we start by characterizing the dynamics and CFC properties of the model in the input landscape.

2.1 Dynamics and Cross-Frequency Coupling in the LaNMM

To analyze the dynamics of the model—prior to our implementation of the Comparator function—we first obtained the bifurcation diagram of the model as a function of mean inputs to the two pyramidal populations. Figure 2 presents the two-parameter bifurcation diagram of the model for (μ_{P_1}, μ_{P_2}), with other parameters as in Sanchez-Todo et al. (2023).[86] Starting at $\mu_{P_1} = 0$, the system exhibits a stable fixed point and evolves toward a steady state. Along the x-axis for $\mu_{P_2} = 0$, the system undergoes a saddle-node on an invariant cycle (SNIC) bifurcation around $\mu_{P_1} \approx 104$ (depicted in green), after which it transitions to periodic dynamics. Increasing μ_{P_1} further leads to two Fold of Limit Cycles (FLC) bifurcations, represented by the dashed red lines. Finally, around $\mu_{P_1} \approx 364$ the periodic dynamics disappear at a supercritical Hopf bifurcation HB_1^+ (purple).

This bifurcation scenario closely resembles that of the coupled Jansen-Rit model discussed in.[103] Notably, without external inputs to P_2, the system is unable to generate gamma rhythms within this range. While the overall structure remains consistent as μ_{P_2} increases, an additional supercritical Hopf bifurcation HB_2^+ (gray) emerges. Of particular interest is the region where two limit cycles coexist, leading to a torus bifurcation (TR) and subsequently driving the system into a quasi-periodic regime. The white dot marks the mean input parameter values used in Sanchez-Todo et al. (2023),[86] $(\mu_{P_1}, \mu_{P_2}) = (200, 90)$ Hz. The black dot indicates the values chosen for this study, $(\mu_{P_1}, \mu_{P_2}) = (270, 90)$ Hz, used in recent modeling work on psychedelics and AD.[104]

Next, we analyze the cross-frequency properties of the model. *Signal-envelope coupling (SEC)*—which is related but not equivalent to PAC[88,105–109] — can be used to implement the error evaluation/comparison process $\mathcal{E}$ at relatively fast time scales (dictated by the low-frequency signal). Here, a slower oscillatory rhythm (encoding predictions) modulates the envelope (or the overall magnitude) of faster oscillations (encoding the incoming sensory data) at the slower timescale. This mechanism allows the slower predictive oscillation to interact with information encoded in the fast oscillation at a "coarse-grained" level, where discrepancies are identified. Both the phase and the instantaneous value of the slower oscillation impact this modulation, aligning the processing of fast inputs with the slower rhythm and enabling the system to compute the necessary error signal.

Envelope-Envelope Coupling (EEC), sometimes referred to as Amplitude-Amplitude Coupling (AAC) or power coupling, can act as a suppression or *gating mechanism at a slower timescale*, which acts by modulating the envelope of faster oscillations according to the envelope of a slower rhythm. This coupling creates windows of increased or decreased excitability, effectively allowing or restricting the propagation of error signals based on the slow oscillatory envelope. Through this gating function, EEC facilitates selective routing by maintaining or suppressing the transmission of specific error signals, extending routing effects over broader timescales. This mechanism we associate with the modulation of prediction error signaling to effectively broadcast precision-weighted prediction errors. EEC allows predictive coding circuits to remain dynamically sensitive to shifts in attentional or contextual relevance. By sustaining periods of high or low excitability based on slower rhythmic inputs, EEC supports long-term gating of

information flow, ensuring that predictive models align with high-level task demands or goals (e.g., attention, vigilance). However, EEC can also be used as a graded inhibitory mechanism capable of encoding contextual information to be contrasted with the input power at longer timescales.

From a statistical perspective, the greater integration time is mandated by the need to accumulate evidence for the precision of prediction errors. This follows because the estimation of precision requires the pooling of instantaneous prediction errors over time (in the same way that a statistician would pool prediction errors over multiple observations to estimate the standard error of her estimated effect size).

The LaNMM model as described in Sanchez-Todo et al. (2023)[86] was used to investigate the interactions between the two pyramidal populations in the neural mass, designated as P_1 and P_2, under varying external inputs $\varphi_{e1}(t)$ and $\varphi_{e2}(t)$. The starting point was the analysis of SEC and EEC.

Simulations were conducted across a two-dimensional parameter space by performing a sweep over the mean input values μ_{P_1} and μ_{P_2} for P_1 and P_2, respectively. For each combination of (μ_{P_1}, μ_{P_2}), the LaNMM was integrated over a predefined timespan using numerical solvers, and the initial transient dynamics were excluded from the analysis by discarding the initial segments of the simulation. The resulting time series of membrane potentials $u_{P_1}(t)$ and $u_{P_2}(t)$ were stored for subsequent analysis (all analysis was carried out using membrane potentials).

EEC was quantified by computing the Pearson correlation coefficient between the amplitude envelopes of P_1 in the alpha band $(8 - 12\,\text{Hz})$ and P_2 in the gamma band $(30 - 50\,\text{Hz})$. SEC was similarly assessed by correlating the band-pass alpha band signal of P_1 with the amplitude envelope of P_2's gamma signal.

Additionally, the power within the alpha and gamma bands for both populations was calculated using both a band-passed Hilbert transform and Welch's power spectral density estimation. These power metrics provide insight into the oscillatory behavior and energy distribution across the specified frequency bands under different input conditions.

Simulations were performed by sweeping μ_{p1} and μ_{p2} over a range from 50 to 400 in steps of 5 Hz. For each parameter pair, we integrated the LaNMM model using a fixed time step ($\Delta t = 1$ ms) and a total simulation time of ∼90 s, discarding an initial transient. Depending on the desired drive condition, the model was run in one of three modes: P_1 drive, P_2 drive, or PV drive. External inputs were generated using a multiscale noise generator that produces a slow random-walk drift and a fast white-noise component (see Appendix G), which were injected into the appropriate population (either P_1, P_2 or, via an extra glutamatergic synapse, PV). For each simulation, we computed coupling metrics: specifically, the correlations between the band-pass-filtered P_1 signal (or its envelope) in the alpha band (8–12 Hz) and the envelope of the P_2 gamma band (30–50 Hz) signal, yielding the SEC and EEC values. In addition, we computed the Population Excitation-Inhibition Index (PEIX) to characterize the saturation of fast and slow oscillatory activity in the model to complement the bifurcation analysis and others (SEC, EEC and power, see Appendix A for details). Maps of the coupling metrics, band power, and

PEIX as a function of mean input to the two pyramidal populations were generated.

2.2 Comparator I: Implementation Using SEC

2.2.1 Error suppression

We can formulate a first hypothesis, regarding the implementation of the comparator with the LaNMM: for a given input, if the correct prior is applied (i.e., a prior alpha signal matching the gamma envelope of the input signal), the output error should be low, which can be measured using the power of the P_2 output envelope—see Figure 3.

To demonstrate this, we created synthetic signals to be used as input and prior messages. The input signal was generated by amplitude modulating a 40 Hz carrier signal with an alpha-band (8–12 Hz) envelope extracted from filtered white noise. To ensure non-zero values, a constant offset was added to the envelope and the carrier wave. The prior signal was designed to either match this alpha envelope (match condition), remain constant (flat condition), or originate from an independent alpha source (wrong condition). These conditions allowed us to investigate the role of input-prior alignment in modulating the network's response.

Given that P_1 is an excitatory population and that the SEC for P_1-driving inputs is positive (see Figure 4), we expected—and confirmed—that for effective suppression of the input signal in the match condition, the prior signal had to be phase-shifted by 180° (i.e., inverted). This inversion allowed the prior to counteract the excitatory input effectively. In contrast, for the PV population, which is inhibitory and has positive SEC for PV-driving inputs, the prior had to be applied in phase with the input signal to achieve suppression. Further details on the variation of power suppression depending on the phase of the matching prior are shown in Appendix C.

These signals were then used to drive the LaNMM. The generated signals were applied as inputs, modifying the membrane potential perturbation u_n of the corresponding populations. The inputs and priors were scaled by gain factors $G_{\mathcal{I}}, G_{\mathcal{P}}$. Simulations were run for a total duration of 100 seconds with a sampling frequency of 1000 Hz.

After running the model, the membrane potential perturbation of the P_2 population, u_{P2}, was extracted and analyzed. This output signal was band-pass-filtered between 30 and 50 Hz to isolate gamma activity, and its envelope was computed using the Hilbert transform. The envelope P_2 signal was then further filtered in the alpha-band (8–12 Hz) to extract the error signal ($\mathcal{E}$). Finally, the power of this alpha-band signal was computed as a measure of error power, allowing us to quantify the impact of different prior conditions on the suppression of mismatch signals.

We first optimized the gain factors $G_{\mathcal{I}}, G_{\mathcal{P}}$ to determine the conditions that resulted in maximal suppression of the error signal in the "match" condition. This optimization was performed by varying the gains and evaluating the resulting error power. The detailed methodology used to compute the gain values is reported in Appendix B.

Using these optimized parameters, we ran ten simulations using different seeds to generate the signals and compared the power of the error signal across the different prior conditions. This

analysis allowed us to assess the extent to which the alignment between the prior and the input influenced the suppression of mismatch-related activity within the model.

2.2.2 Computation of prediction error

The above study is a special case of a more general statement: for a given input signal encoding a message (in the gamma envelope) and a given prior signal encoding a different message (as an alpha band oscillation), the output signal (encoded as the gamma envelope of the P_2 output) will approximate the difference of the signals, i.e., a prediction error approximation.

The hypothesis can be formalized as $\mathcal{E} = a \cdot \mathcal{I} + b \cdot \mathcal{P} + \hat{\eta}$, where $\mathcal{E}$ is the P_2 output envelope (and prediction error estimate) produced by the LaNMM, as explained in the previous section, $\mathcal{I}$ is the input message (fast oscillation envelope), $\mathcal{P}$ is the prior message (slow oscillation signal), and $\hat{\eta}$ denotes unmodeled noise. Here, a and b are constants (real numbers) that scale the input and prior, respectively, and we expect a and b to be of opposite sign (subtraction).

To determine a and b, we optimize the loss function

$$\mathcal{L}(a, b) = ||\mathcal{E}(\mathcal{I}, \mathcal{P}) - (a \cdot \mathcal{I} + b \cdot \mathcal{P})||^2 \tag{2}$$

Using this loss function, we find a and b with which the LaNMM output is best approximated as a linear function of input and prediction.

To demonstrate that the minimal loss is meaningful, we define an alternative loss function,

$$\mathcal{L}'(a, b) = ||\mathcal{E}(\mathcal{I}, \mathcal{P}) - (a \cdot \mathcal{I} + b \cdot \mathcal{X})||^2 \tag{3}$$

where $\mathcal{X}$ denotes a random assignment of mismatched predictions. We can then verify that, for a given pair $(\mathcal{I}, \mathcal{P})$ used as input and prediction to the LaNMM, the minimization of $\mathcal{L}$ results in a lower loss than the minimization of $\mathcal{L}'$. We assume that the unrelated priors $\mathcal{X}$ are instantiations of different alpha signals with the same mean and amplitude as the priors sent to the LaNMM, obtained with different seeds.

To generate information-rich output and subtraction messages and avoid power suppression of the input, the signals used as priors did not match the input signals (i.e., they were generated with different seeds than the input, corresponding to the "wrong" prior case in the previous section).

We generated ten such pairs of $(\mathcal{I}, \mathcal{P})$ and ten unrelated priors $\mathcal{X}_i$ for each pair, and minimized $\mathcal{L}$ and $\mathcal{L}'$ in each case. To understand whether the error computed with the LaNMM was best approximated by a linear combination of $(\mathcal{I}, \mathcal{P})$, we ran an independent samples t-test comparing the distribution of $\mathcal{L}$ and $\mathcal{L}'$ values. We carried out this study for the prior sent to the P_1 population and for the prior sent to the PV population.

2.3 Comparator II: The role of EEC for precision weighting

Here, we study the idea that EEC (anticorrelation) can be used to modulate the precision of prediction errors within the column—see Figure 3. We assume that the precision of prediction errors, $\Pi_{\mathcal{E}}$, is encoded in their lower-frequency envelope (longer timescale averaged power) and show how EEC can be used to amplify or attenuate the precision of error by applying top-down precision-modulation signals $\Pi_{\mathcal{P}}$. Implicitly, we assume that the confidence in inputs (the precision of the incoming error from bottom-up layers), $\Pi_{\mathcal{I}}$, is encoded in the amplitude of their envelopes, too.

As input signal, we used a non-modulated 40 Hz carrier signal with mean 2 mV and amplitude 2 mV, to ensure that the input was always positive. To obtain a precision-modulation signal, we created a random square wave of 100 seconds by adding 5 random steps of duration 10 seconds and amplitude 1 mV to a flat signal of 1 mV. Such a square wave represents the input precision $\Pi_{\mathcal{I}}$. We amplitude-modulated a 10 Hz carrier signal to obtain the precision-modulation signal. We added a constant offset of 2 mV to the resulting signal to ensure non-zero values. To evaluate the effect of the precision-modulation signal, we used as a contrast condition a "flat" precision-modulation signal (no modulation) oscillating at 10 Hz (with mean 2 mV and 2 mV amplitude).

As before, the inputs and priors were scaled by gain factors $G_{\mathcal{I}} = 1, G_{\mathcal{P}} = 10$, which were optimized to result in maximal modulation of the error precision (such optimization is detailed in Appendix B).

After running the model, the membrane potential of the P_2 population was extracted and analyzed. The output signal was band-pass-filtered between 30 and 50 Hz to isolate gamma activity, and its envelope was computed using the Hilbert transform. The envelope P_2 signal was then further low-pass filtered below 1 Hz to extract the error signal precision ($\Pi_{\mathcal{E}}$). Finally, the gamma power of the P_2 output was computed and compared for the precision-modulation and flat modulation signals as a measure of error attenuation. We ran ten simulations using different seeds to generate the signals and evaluated the difference across conditions using paired t-tests.

2.3.1 Modulation of precision

Here we aim to show that for a given input signal encoding a message with some precision $\Pi_{\mathcal{I}}$ (in the slow envelope of gamma) and a given prior signal encoding some precision modulation $\Pi_{\mathcal{P}}$ (in the alpha signal envelope), the output signal will encode an approximate subtraction of the respective precisions, reflected in the slow envelope of the P_2 output.

In this case, we used as input messages signals with varying precision $\Pi_{\mathcal{I}}$, obtained in the same way as the precision-modulating signals described in the previous section. Prior messages encoding the precision modulation were obtained in the same way.

We observed that such simple input and prior messages of amplitude 1 mV, the normalized P_2 output slow envelope (between -1 and 1), $\hat{\Pi}_{\mathcal{E}}$, approximates the direct subtraction of input and

prior precisions well. We thus computed the MSE between the slow envelope of the P_2 output and the subtraction of input and prediction precisions (long time scale envelopes),

$$\mathcal{L} = ||\hat{\Pi}_{\mathcal{E}}(\mathcal{I}, \mathcal{P}) - (\Pi_{\mathcal{I}} - \Pi_{\mathcal{P}})||^2 \tag{4}$$

We will refer to this as the *consistent* case since the input and prediction provided to the LaNMM are the ones used in the subtraction to compute the MSE.

To demonstrate that such MSE obtained is meaningful and that the modulation computed by the LaNMM approximates the subtraction of input and prior precision well, we can also compute the MSE between the LaNMM output slow envelope and the subtraction of input and an unrelated prior precision $\Pi_{\mathcal{X}}$ (inconsistent case),

$$\mathcal{L}' = ||\hat{\Pi}_{\mathcal{E}}(\mathcal{I}, \mathcal{P}) - (\Pi_{\mathcal{I}} - \Pi_{\mathcal{X}})||^2 \tag{5}$$

The unrelated prior precision $\mathcal{X}$ is constructed in the same way as the prior sent to the LaNMM but with another seed to define the random signal generation.

As in the SEC case, the signals used as priors did not match the input precision signals (i.e., they were generated with different seeds than the input, corresponding to the "wrong" prior case in the previous section). We generated 10 pairs of $(\mathcal{I}, \mathcal{P})$ to be used as input and prior to the LaNMM and one unrelated prior $\mathcal{X}$ for each pair, and computed $\mathcal{L}$ and $\mathcal{L}'$. To understand whether the error computed with the LaNMM approximated the subtraction well $\Pi_{\mathcal{I}} - \Pi_{\mathcal{P}}$, we ran a paired t-test comparing the distribution of MSE values for the consistent and inconsistent cases.

2.4 Disruption of Comparator Function

2.4.1 Serotonergic Psychedelics

We then studied disruption of the comparator function due to the interaction with classical serotonergic psychedelics (*psychedelics* hereafter). The excitatory effects of psychedelics were implemented in the model as an increase in the excitatory synaptic gains, W_{exc}, of the P_1 population, based on previous modeling work.[104] See also the empirical changes in excitability estimated using dynamic causal modelling in (Muthukumaraswamy et al., 2013).[110]

We first analyzed the alterations induced by psychedelics in the oscillatory behavior of the LaNMM by computing the alpha and gamma power of the P_1 and P_2 populations for different values of the W_{exc} parameter. Based on those results, we chose a value of $W_{exc}^{\Psi} = 4.5$ mV to represent the acute phase of psychedelics. For this value, the alpha power in the P_1 population was strongly reduced in the model, while the gamma power in the P_2 population was substantially increased.

We analyzed the effects of these alterations in the LaNMM computation of prediction error using the SEC and EEC mechanisms. We first computed the power of the error signal (P_2 output gamma envelope) obtained in the SEC scenario in the *baseline* condition ($W_{exc}^{0} = 3.25$ mV, default value in the LaNMM and in Jansen-Rit[83,86,104]) and the *psychedelics* condition, in

the case where a prior matching the input was applied.

We then studied the alterations in the EEC mechanism for precision computation. As in the SEC case, we computed the gamma power of the error signal (P_2 output slow envelope) in the baseline condition and the psychedelics condition, in the case where a 10 Hz precision-modulating signal was applied to P_1.

2.4.2 PV+ disinhibition in Alzheimer's Disease

The inhibitory deficits associated with AD were implemented in the model as a reduction in the strength of inhibitory synaptic connections from the PV population to the P_2 population, $C_{PV \to P2}$, based on previous computational models of AD-related dysfunction.[111]

We first analyzed the alterations induced by AD in the oscillatory behavior of the LaNMM by computing the alpha and gamma power of the P_1 and P_2 populations for different levels of PV dysfunction. Based on the work in Sanchez-Todo et al. (2024),[111] we selected a level of inhibition reduction for different stages of disease progression: healthy (baseline value, $C_{PV \to P2} = 550$), Mild Cognitive Impairment (MCI) ($C_{PV \to P2} = 300$) and AD ($C_{PV \to P2} = 140$).

We first evaluated the alpha and gamma power alterations in the different stages of AD due to variations in the $C_{PV \to P2}$ parameter. We then analyzed the effects of these alterations in the LaNMM computation of prediction error using the SEC and EEC mechanisms.

We computed the power of the error signal (P_2 output gamma envelope) obtained in the SEC scenario for each AD stage, using a prior matching the input. We then studied the alterations in error precision computation using EEC. As before, we used a flat input oscillating at 40 Hz and a prior signal encoding some precision-modulation oscillating at 10 Hz. We computed the power of the error signal in each AD stage as a measure of the EEC error suppression by the precision-modulating signal.

3 Results

3.1 The LaNMM Sustains Robust SEC and EEC for a Wide Range of Mean Inputs

We began by examining the behavior of the system when random inputs were presented to P_1, P_2, and PV. Figure 4 displays maps indicating the mean positive SEC and negative EEC values. These results reveal that in a wide range of configurations, the system naturally yields the desired combination of positive SEC and negative EEC. This provides a baseline for how the laminar model processes random inputs before introducing comparator mechanisms.

The results of the simulation of SEC and EEC highlight the robustness of EEC and SEC couplings across wide ranges of the parameter space. As a result of robust EEC with P_1 driving (Figure 4), we see that envelope coupling provides a mechanism for suppression of competitive oscillations. For example, alpha power (evaluated by its envelope) can be used to suppress the gamma envelope or vice versa. However, the same applies in the other direction: fast oscillation

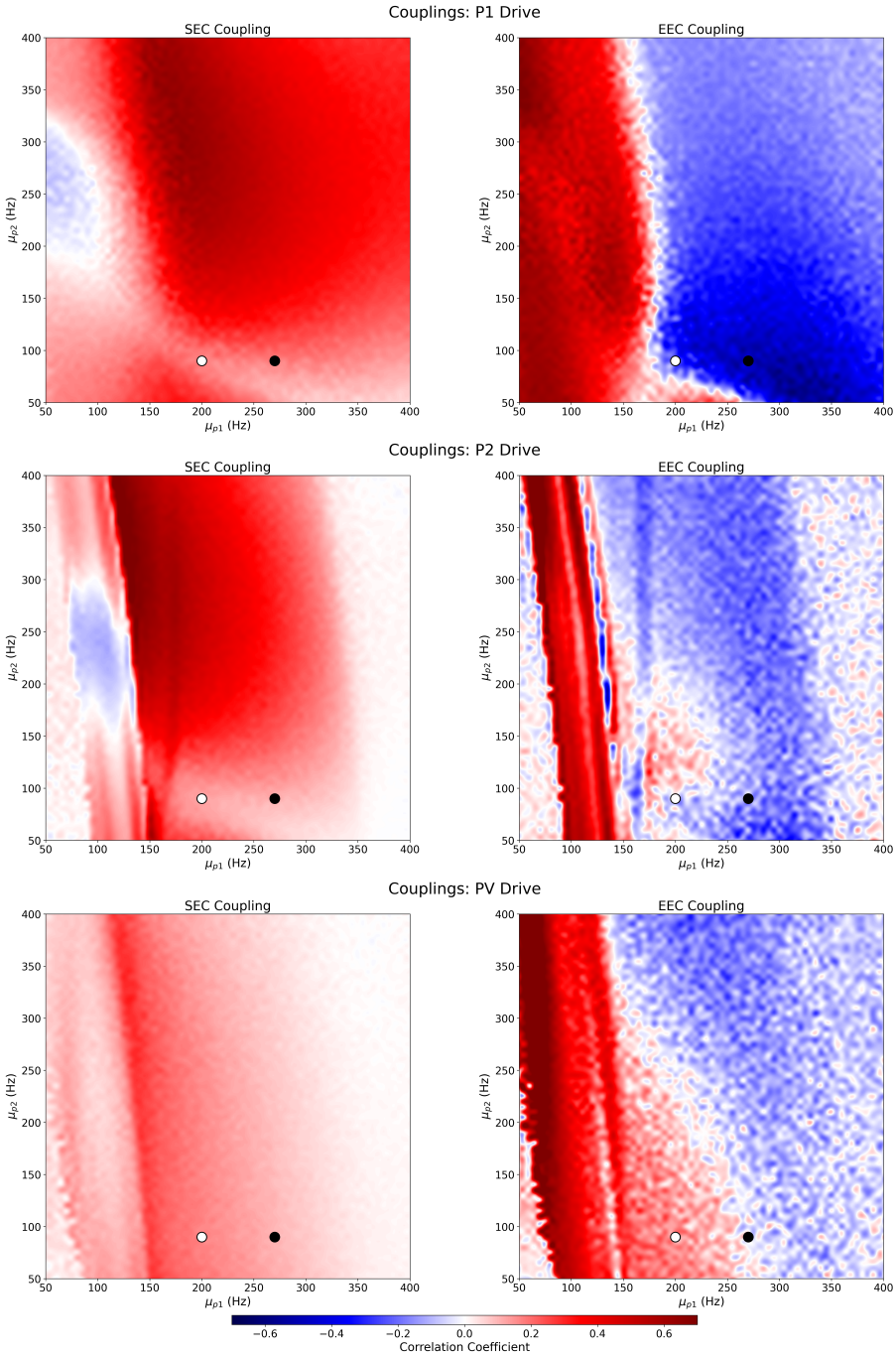

Figure 4: SEC (left column) and EEC (right) between neural populations P_1 and P_2 for random inputs to P_1 (top row), P_2 (middle), and PV (bottom). Both P_1 and P_2 receive a constant mean external drive (x and y axis), with zero mean noise injected into one of them via a glutamatergic synapse. This dual-input strategy allows the model to capture both the steady excitatory drive and the stochastic fluctuations affecting the desired population. The right column displays the correlation between the alpha envelope of P_1 and the gamma envelope of P_2 (EEC), while the left column depicts the correlation between the alpha signal of P_1 and the gamma envelope of P_2 (SEC). The white dot marks the mean input parameter values used in Sanchez-Todo el al. (2023),[86] $(\mu_{P_1}, \mu_{P_12}) = (200, 90)$ Hz. The black dot indicates the values chosen for this study, $(\mu_{P_1}, \mu_{P_2}) = (270, 90)$ Hz.

power can be used to regulate slow oscillation activity. This mechanism can subserve gating by inhibition and predictive routing, as is further discussed below. Figures A1 and A2 in the Appendix display maps of the computed power within the alpha and gamma bands for both P_1 and P_2, revealing how power distributions vary with changes in the external drives μ_{P_1}, μ_{P_2} and μ_{PV}.

3.2 SEC subserves Fast-Time Comparator Function

We first employed the SEC mechanism to implement the Comparator function (i.e., the difference between input and prior). Two primary configurations were tested: providing the prior to P_1 and providing the prior to PV. Figure 5 illustrates the suppression of error signal power in the first case. The second configuration (prior to PV) is shown in Figure 7, demonstrating that both achieve a similar comparator function using SEC. Indeed, in both cases, sending a prior signal matching the input signal results in lower error power than sending a flat prior or a wrong prior.

Figure 6 illustrates the computation of prediction error when the prior is provided to the P_1 population. The results for the PV configuration are shown in Figure 8. As shown in Figures 6d and 8b , the loss value with the original prior is always lower than the loss value with alternative priors. This demonstrates that the linear combination of the input and prior signals sent to the LaNMM explains the LaNMM output better than the combination of the input with other arbitrary prior signals (i.e., that $\mathcal{L}^*$ is minimal).

3.3 EEC subserves Slow-Time Precision Modulation

Figures 9 depicts how EEC suppresses the precision of error signals: the error signal is significantly attenuated (lower error power) when using a precision-modulating signal with transient increases in alpha power (slow envelope), as opposed to the case where a flat, non-modulating prior is sent to $P1$.

Figure 10 illustrates how EEC in the LaNMM can be used to perform modulation of prediction errors by subtraction. The error signal precision encodes the difference between the input precision and the precision-modulating prior signal, as quantified by the MSE between the normalized error precision and the subtraction of the $\Pi_{\mathcal{I}}$ and $\Pi_{\mathcal{P}}$. The similarity between the LaNMM output ($\mathcal{E}$ precision, $\Pi_{\mathcal{E}}$) and the subtraction of input and prior precisions ($\Pi_{\mathcal{I}} - \Pi_{\mathcal{P}}$) is illustrated in Figure 10b. Overall, the results indicate that EEC can be harnessed to modulate the precision of error signals.

3.4 Psychedelics and Interneuron Pathology Disrupt the Comparator

Finally, we investigated how LaNMM disruptions associated with serotonergic psychedelics or Alzheimer's Disease interneuron pathology impact the comparator functions.

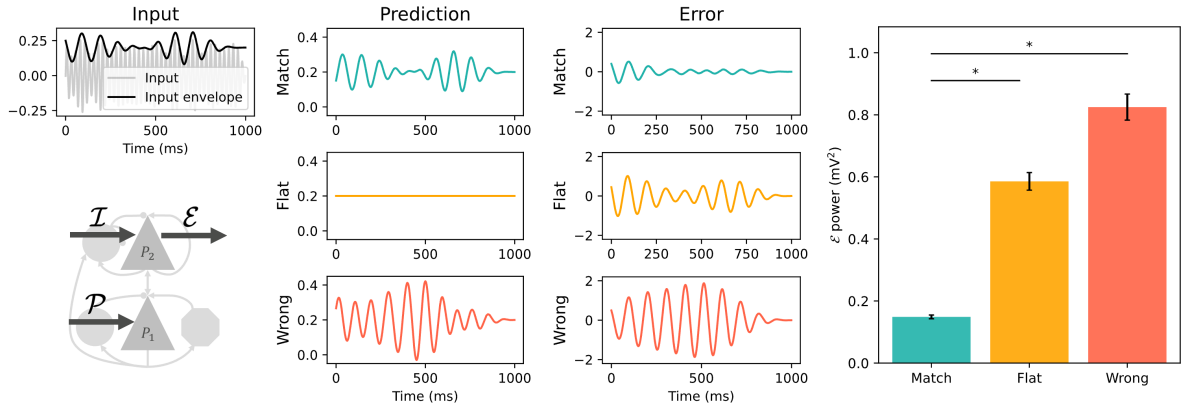

Figure 5: SEC suppression scheme, prediction sent to $P1$. If the prediction signal matches the input (blue traces), the error signal—P_2 output envelope—is suppressed, as shown by the reduced power (right bar plot). We compare the case of a matching prediction with the case of a flat prediction signal (orange traces) and a wrong prediction signal (red traces). The asterisk denotes a significant difference over multiple simulations in a paired t-test ($p < 1e^{-5}$), a convention followed in all subsequent figures.

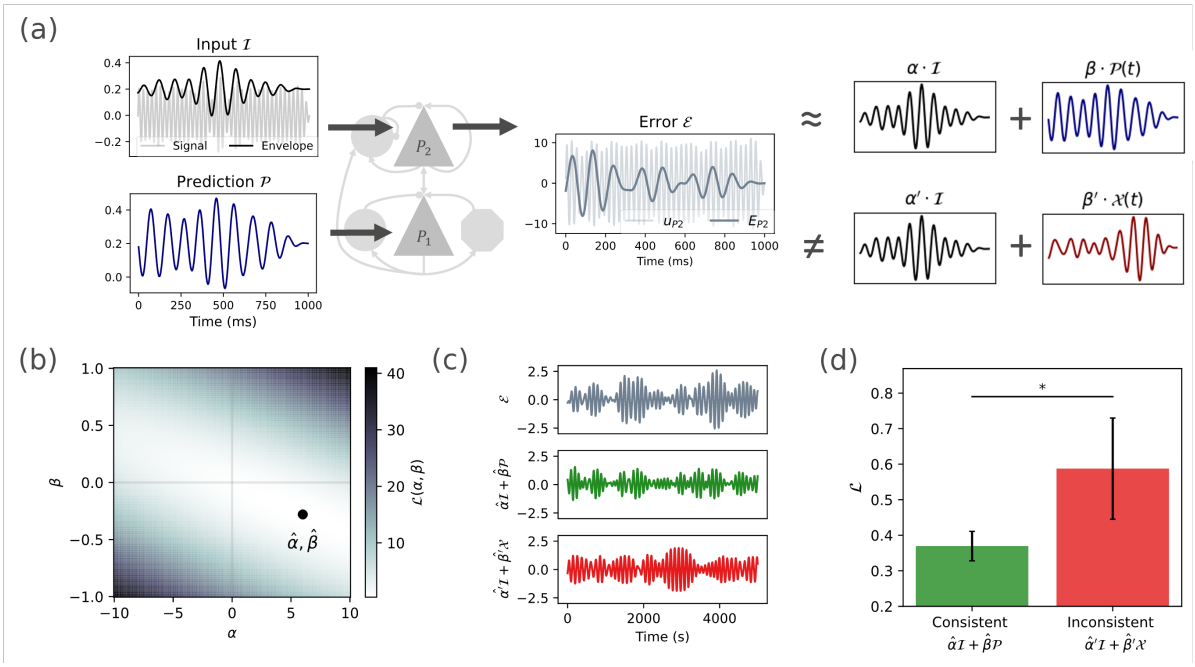

Figure 6: SEC subtraction scheme, prediction sent to $P1$. (a) Study hypothesis: we can find a linear combination of the input and prediction signals $\alpha \cdot \mathcal{I}(t) + \beta \cdot \mathcal{P}(t)$ that approximates the error signal, with α and β of different sign (subtraction). Using an unrelated signal $\mathcal{X}(t)$ for the linear combination leads to a worse approximation. (b) Optimal values $\hat{\alpha}, \hat{\beta}$ for a specific pair $(\mathcal{I}, \mathcal{P})$. The loss function $\mathcal{L}$ is defined as the MSE between the error signal and the linear combination of input and prediction. (c) The error computed by the LaNMM (grey traces) is well approximated by the optimal subtraction of input and prediction (green traces) but not by the optimal subtraction of the input and an unrelated signal (red traces). (d) The optimal subtraction using $\mathcal{I}$ and $\mathcal{P}$ (consistent case) is closer to the LaNMM output (minimal $\mathcal{L}$ value) than the optimal subtraction using an I and an unrelated signal $\mathcal{X}$ (inconsistent case).

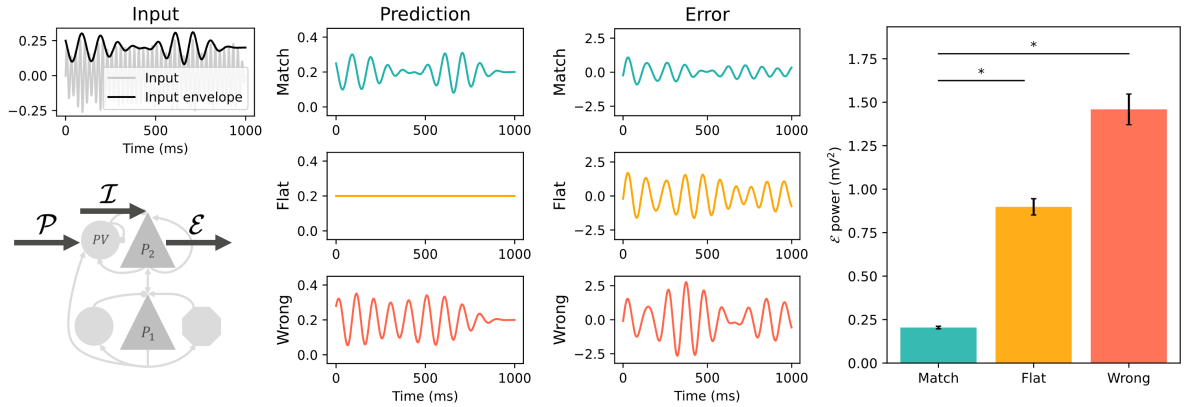

Figure 7: SEC suppression scheme, prior sent to PV. If the prediction signal matches the input (blue traces), the error signal—P_2 output envelope—is suppressed, as shown by the reduced power (right bar plot). We compare the case of a matching prediction with the case of a flat prediction signal (orange traces) and a wrong prediction signal (red traces). The asterisk denotes a significant difference over multiple simulations in a paired t-test ($p < 1e^{-5}$).

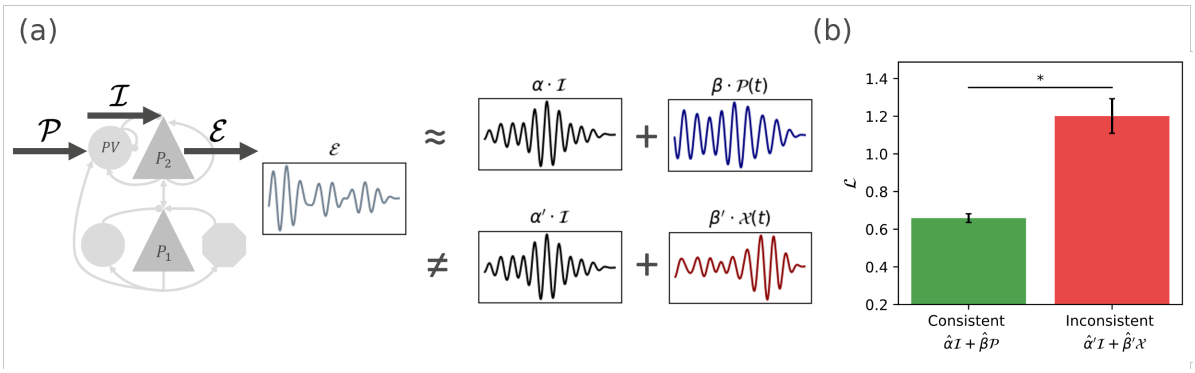

Figure 8: SEC subtraction scheme, prior sent to PV population. (a) Study hypothesis: we can find a linear combination of the input and prediction signals $\alpha \cdot \mathcal{I}(t) + \beta \cdot \mathcal{P}(t)$ that approximates the error signal, with α and β of different sign (subtraction). Using an unrelated signal $\mathcal{X}(t)$ for the linear combination leads to a worse approximation. (b) For a given input $\mathcal{I}$ and prediction $\mathcal{P}$ received by the LaNMM, the optimal subtraction using $\mathcal{I}$ and $\mathcal{P}$ (consistent case) is closer to the LaNMM output (minimal $\mathcal{L}$ value) than the optimal subtraction using an I and an unrelated signal $\mathcal{X}$ (inconsistent case). The asterisk denotes a significant difference over multiple simulations in an independent samples t-test ($p < 1e^{-5}$).

3.4.1 Serotonergic Psychedelics

Figure 11 illustrates how the increased excitability due to serotonergic psychedelics, reflected in the model by an increase of the parameter W_{exc}, translates into power spectrum alterations and the disruption of the comparison process. In particular, we can see how the low prediction error resulting from a matching input and prior in the baseline condition (low P_2 envelope power) is increased in the psychedelics condition, resulting in an error similar to the one obtained when a flat prior is applied (see Figure 5). Moreover, under the psychedelics condition, the influence of the precision attenuation signal is greatly reduced, causing the error to increase and primarily reflect the input signal.

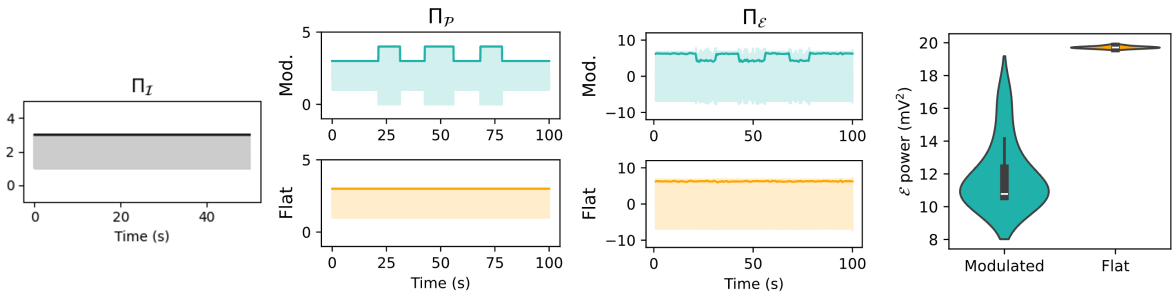

Figure 9: EEC suppression scheme. The precision modulation signal presented to P_1, $\Pi_{\mathcal{P}}$, successfully attenuates the error precision $\Pi_{\mathcal{E}}$ (P_2 output slow envelope). The error precision is reduced by the precision-modulation signal, as shown by the reduced error power (right violin plot). We compare the case of a precision-modulation signal (blue traces) with the case of a flat precision-modulation signal (orange traces, no modulation).

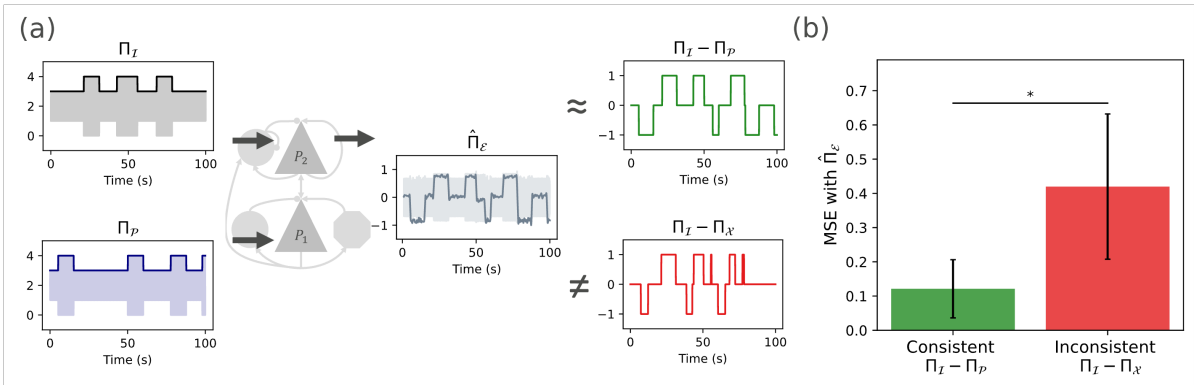

Figure 10: EEC subtraction scheme. (a) The error signal precision encodes the difference between input precision and prior precision. (b) For a given input and prior encoding some precision modulation sent to the LaNMM, the output error precision is better approximated by the difference $\Pi_{\mathcal{I}} - \Pi_{\Pi}$ (consistent case) than by the difference between the input precision and unrelated modulation-precision signal $\Pi_{\mathcal{I}} - \Pi_{\mathcal{X}}$ (inconsistent case), as captured by the MSE between the LaNMM output $\hat{\Pi}_{\mathcal{E}}$ and the subtraction of each case.

Overall, these results suggest that serotonergic psychedelics increase the effective weight of inputs due to increased power of fast (gamma) oscillations, and diminish the effect of predictions and precision-modulating signals, as a consequence of the reduced power in slow (alpha) oscillations. This results in higher prediction error signals in the psychedelics condition.

3.4.2 Alzheimer's Disease

Figure 12 illustrates how positive SEC/negative EEC patterns and comparator functionality degrade under AD-disrupted predictive coding conditions. The alteration of the $C_{PV \to P_1}$ parameter leads to an increase in alpha and gamma power in early stages (hyper-excitability) and an overall power decrease in late stages.

In both the MCI and AD stages, we find that the error evaluation process is disrupted with respect to the healthy stage. In particular, the low prediction error obtained through SEC for a matching input and prior is strongly increased in MCI stage and then slightly increased in

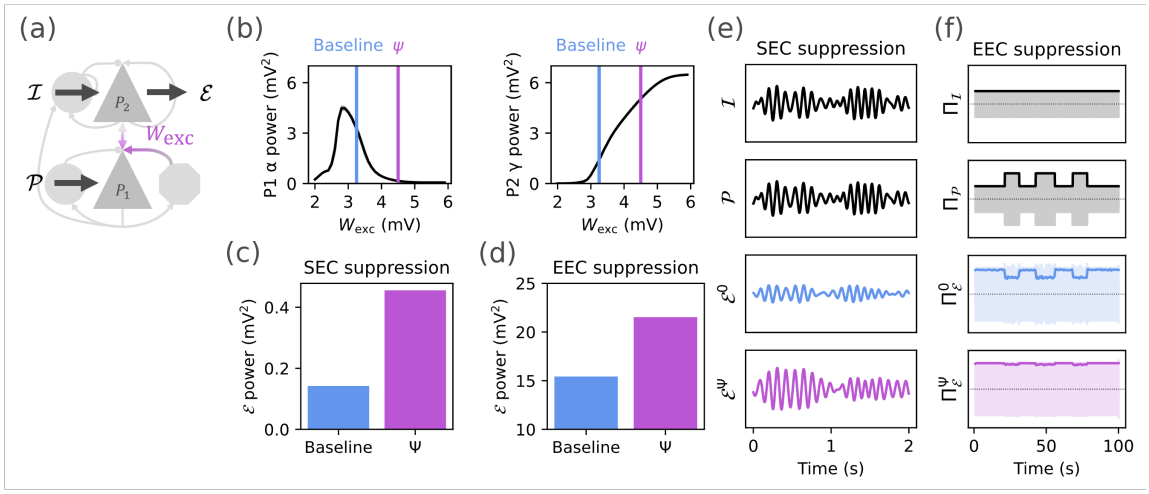

Figure 11: Effects of serotonergic psychedelic alterations on the LaNMM model. (a) The excitatory effects of serotonergic psychedelics are implemented as an increase of the excitatory synaptic gains, W_{exc}, of the P_1 population.[104] (b) The alteration of W_{exc} in the model leads to decreased alpha power and increased gamma power. (c) For the SEC mechanism, the error suppression for a prediction matching the input is altered by psychedelics, resulting in a higher power of the error signal. (d) For the EEC mechanism, the influence of the precision-modulating signal is diminished, also resulting in increased error. (e, f) Example signals illustrating the SEC (e) and EEC (f) comparator mechanism for the baseline and psychedelics condition, showing a reduced effect of the prior and precision-weighting modulation in the psychedelics condition.

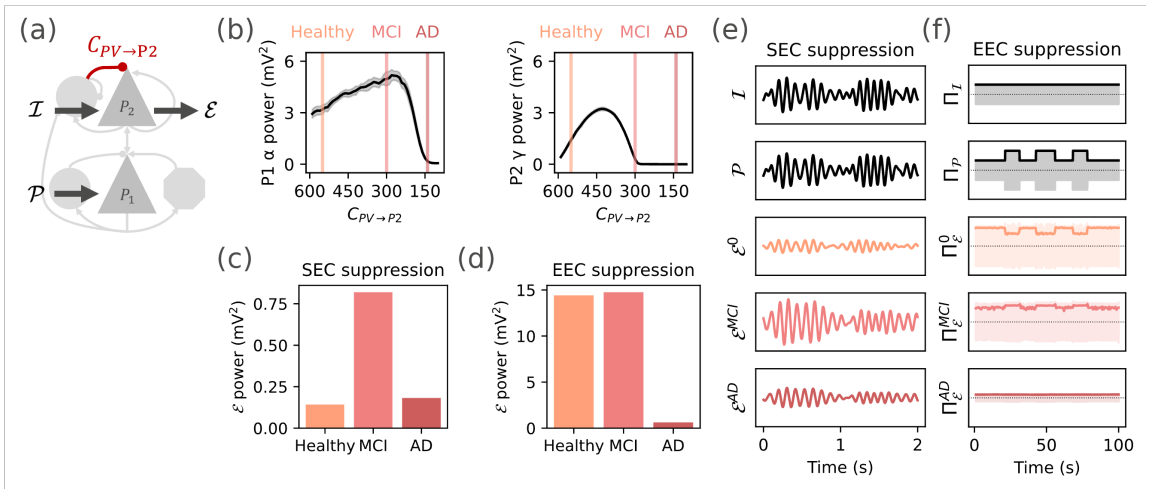

Figure 12: Effects of AD-like pathological alterations on the LaNMM model. (a) AD pathology is introduced by reducing the connectivity of the PV+ to P_2 population, $C_{PV\to P_1}$.[111] (b) The alteration of $C_{PV\to P2}$ reflects the different stages in the progression to AD and leads to an increase in alpha and gamma power in early stages and an overall power decrease in late stages. (c) The suppression of prediction error observed in the healthy stage for matching input and prediction is disrupted in AD stages (especially MCI), resulting in higher prediction errors. (d) The effect of the precision-modulating signal is reduced in the MCI stage, resulting in higher error power, while in the AD stage, the error power is substantially diminished. (e, f) Sample signals illustrating the SEC (e) and EEC (f) comparator mechanism for the baseline and altered conditions, showing a reduced effect of the prior and precision-weighting modulation in the altered condition.

the AD stage with respect to the healthy condition (Figure 12c). The low prediction error power observed in AD reflects Comparator dysfunction: the similarity in error power between AD and healthy conditions arises not from accurate prediction, but rather from an overall reduction in cortical power typical of AD, as illustrated by decreased alpha and gamma activity in Figure 12b.

This is confirmed by the case of the EEC mechanism—panels (d) and (f)—, where the effect of a precision-modulating signal is reduced in the MCI condition (higher prediction error as well), but the error power is drastically reduced in the AD stage (Figure 12f).

In sum, these results suggest that in the early stages of AD, error evaluation and precision are disrupted (increased prediction error computation and reduced influence of precision-modulating signals), leading to higher prediction errors even when signals match. In later stages, prediction errors are abnormally suppressed regardless of predictions or the modulation of precision by top-down signals.

4 Discussion

4.1 Interpretation of results

Our modeling results show that it is possible to implement the evaluation of $\mathcal{E}$ in various ways using the cross-frequency properties of the LaNMM, with an information encoding scheme where information is stored in signals or in their envelopes.

We first showed how the model, both in its nominal parametrization[86] and in a wider mean input landscape, provides robust bidirectional cross-frequency coupling: controlling the input fluctuations into P_1, P_2 or PV results in envelope fluctuations in the other population (P_2, P_1, and PV, respectively) (see Figure 4).

More specifically, we observed robust (positive) SEC, consistent with the previously reported PAC.[86,102] With regard to negative EEC, it is noteworthy how the two subpopulations operate in what we may call *dynamical competition*, a sort of zero-sum game of the total power generated by the column. Cross-frequency coupling provides the basis for the rest of our results, and, in particular, SEC motivates the further exploration of an AM information encoding scheme in neural signals.[100,112]

Exploiting SEC and EEC, we then showed how the evaluation of $\mathcal{E}$ can be carried out by the laminar column. In the first case, information carried by the fast oscillation envelope arriving at P_2 is contrasted with a slow prediction signal, producing effective suppression if the prediction is accurate. Two mechanisms were provided. The first was implemented with the signal predictions arriving at P_1 with a phase shift of $\approx \pi$ with respect to the input signal. In the second implementation, predictions arrived at the PV cell in the PING subpopulation (in phase with the input signal).

In the case of EEC, where information is carried by the "envelope of the envelope" of the fast oscillation at a slower time scale, the prediction is encoded as the envelope of the slower signal

arriving at P_1, without phase shift or sign reversal, and the evaluation is carried out over a longer time scale (determined by the time scale of the envelope of the slow signal). Figure 3 illustrates this scenario.

An instructive analogy with regard to the role of time scales comes from radar signal processing, particularly Synthetic Aperture Radar (SAR), which distinguishes between *fast-time* and *slow-time scales*.[113] In SAR, fast-time corresponds to the rapid reflections of individual radar pulses used for high-resolution range measurements—analogous to rapid signal-to-envelope coupling (SEC) for fast prediction-error computations. Conversely, slow-time relates to the slower progression of the radar platform across multiple pulses, enabling integration of spatial information over a larger scale—mirroring envelope-to-envelope coupling (EEC), which facilitates predictive integration and gating at slower timescales.

4.2 Predictive coding and precision

Our results with EEC provide a mechanism for neural processing proposals hinging on the availability of gating, which is necessary for the Bayesian implementation of predictive coding. Technically, predictive coding was introduced in the 1950s as a scheme for compressing sound files.[114] This is conceptually pertinent to KT in the sense that compression is exactly the objective prescribed by minimizing algorithmic complexity under this framework. In the neurosciences, predictive coding was subsequently applied to continuous (neuronal) signals and state estimation in the brain.[2,115,116] From an engineering perspective, predictive coding for continuous state space models corresponds to Bayesian filtering and, in the limit of linear models, Kalman filtering.[1] The Kalman filtering perspective is important because it reveals that there are two things that need to be estimated in predictive coding: the prediction error *per se* and the (Kalman) gain that is to be applied to the prediction error for model update (see Appendix D). Crucially, the Kalman gain itself has to be optimized, which requires an estimation of the precision (i.e., inverse variance) of sensory and state noise. In short, there are two kinds of elements that need to be predicted in predictive coding: the (first-order) content and the (second-order) precision. This dual aspect inherits directly from the assumption of Gaussian posterior estimates in predictive coding, which have two sufficient statistics, namely, (first-order) mean and (second-order) precision (inverse covariance).

When translating this dual estimation problem into the frequency domain, the current formulation associates this with cross-frequency coupling of a fast and slow sort, respectively (i.e., phase-amplitude or, more generally, SEC, and amplitude-amplitude / EEC coupling). Intuitively, assigning a high precision to a prediction error enables it to have a greater effect on subsequent state estimation or (Bayesian) belief updating. This manifests—in deep or hierarchical models—as an optimal gating of ascending prediction errors, such that precise prediction errors are selected over imprecise prediction errors. When the precision of prediction errors fluctuates, then the implicit selection, routing, or gating acquires a dynamic aspect, resulting in a Bayes-optimal dynamic coordination, routing or gating.

4.3 Gating by Inhibition and Predictive Routing

EEC in the LaNMM can support functions that can be interpreted in terms of gating by inhibition and predictive routing. Gating mechanisms are used to implement fundamental logic gates, the building blocks of all digital computation and self-regulating systems.[117] Gates lie at the heart of every computational system because they enable conditional branching—the capacity to direct information flow according to context.

At its most elementary level, computation is realized by functions $f : \{0,1\}^n \rightarrow \{0,1\}$, where inputs (bits) are mapped to an output bit in a rule-based manner.[118,119] In the simplest non-trivial case, $n = 2$, there are only 16 possible functions from $\{0,1\}^2 \rightarrow \{0,1\}$, including the standard Boolean primitives AND, OR, XOR, NAND, NOR, and so on.[120] A logic gate is nothing more than a controlled "pass" or "block" of a signal, and selectively letting signals through or stopping them is the fundamental mechanism behind digital logic: every "yes/no" decision in a computer boils down to whether a transistor (or switch) is opened or closed.[121] By chaining these yes/no gates together, we build up all of Boolean logic—and thus all the operations a computer performs (sufficient sets are the NAND, or the AND plus NOT). Historically, Babbage's mechanical engines relied on gears and levers as physical switches to select different arithmetic operations.[122] Later, early electronic computers such as Colossus employed vacuum tubes to achieve fast on/off behavior essential to codebreaking.[123] Modern computing systems now integrate billions of transistor-based switches to flexibly control signal routing, forming the basis for reprogrammable logic.[124] In the brain, switching is implemented via inhibitory gating, in which interneurons can switch neural pathways on or off by hyperpolarizing downstream targets or, as discussed here, through competitive oscillations via EEC. This gating provides the same conditional-branching capability seen in electronic hardware: specific signals are allowed or blocked depending on context, supporting attention, learning, and adaptive decision-making.[125] Thus, whether realized with mechanical gears, vacuum tubes, transistors, synaptic inhibition, or oscillatory competition, switching at different spatiotemporal scales is foundational to any system that must selectively route information—and it underscores the shared computational logic between engineered machines and biological neural networks.

Although we have focused on the implementation of the Comparator with information encoded in temporal signals, as a network, the brain also encodes information in space, i.e., where the signals arrive. In the case of local error evaluation, weighted error predictions must arrive at the right location to be effective in suppressing the propagation of errors. That is, agent predictions are in general of the form "these signals will arrive at this location at these times". This expectation may be an active one, where the system reconfigures (via switches, for example) to route information streams in a particular way. Information processing in space and time must, therefore, work together for predictive error evaluation, and the predictions will, in general, be about events in space and time following some actions (actions in the world or network reconfigurations).

In contrast with the local evaluation of prediction error discussed above, *routing*[21] *or gating*[20] in neuroscience refer to the dynamic modulation of information flow across cortical hierarchies, selectively directing or suppressing signal propagation. Together, these processes ensure efficient,

prioritized information flow across brain networks.

Gating mechanisms determine which signals can pass through at any given time and modulate the gain of signals based on relevance or salience. This is sometimes referred to as *gating by inhibition*[20], a framework where optimal task performance correlates with alpha activity in task-irrelevant areas. Gating by inhibition has been proposed as an attentional mechanism, where the agent chooses what information streams to process by selectively dampening or enhancing signals through inhibitory processes.[20] In modern neural network transformer architectures, a similar principle of selective attention is implemented via multi-head attention, which learns to weight different input elements, effectively gating the flow of information in deep networks.[126]

In relation to this, *predictive routing* is a proposed mechanism where top-down predictions dynamically shape sensory information flow by selectively inhibiting expected inputs through amplitude-amplitude coupling (AAC),[21] the equivalent of EEC in our framework. In predictive routing, the brain anticipates incoming sensory data based on prior knowledge and actively suppresses the cortical pathways associated with these predictions. This can be interpreted in light of prediction error evaluation where selective inhibition implements the Comparator in a distributed manner (not on a single column) and on a longer, coarse-grained timescale than SEC, dynamically routing unexpected signals for further processing. In this context, *information is encoded by route* and predictions address the route taken by sensory stimuli: correctly predicted inputs are inhibited, while unpredicted inputs propagate, signaling prediction errors (see Appendix E and Figure E1 for further details). Top-down predictions are communicated via alpha/beta oscillations (8–30 Hz) originating from deep cortical layers. These rhythms prepare sensory pathways by pre-emptively inhibiting the columns that process expected inputs. It is this pre-emptive aspect that reflects predictions of which prediction errors will convey precise or salient information.

The interplay between these dynamics, governed by the laminar organization of the cortex, ensures that deep layers provide the inhibitory feedback while superficial layers relay the feed-forward sensory information. This layer-specific interaction dynamically selects the route for information flow. Thus, EEC provides a mechanism for weighted spatiotemporal information processing of prediction errors as well as other information processing agent choices in network space and time (e.g., attention and sensory attenuation). In all these instances, it reflects the choice and optimal use of *relevant information* for model updates conducive to the maximization of the agent's Objective function.

Finally, in the general KT algorithmic agent framework, modeling, objective functions, and planning are treated as distinct processes. Attention (and action) emerges as a separate gating mechanism that selectively routes information and allocates resources, while precision weighting specifically modulates how prediction errors drive updates in the model. By contrast, in Active Inference, goal optimization is effectively folded into the generative model through prior beliefs, so that modeling, attention, and action all become facets of a single process—minimizing free energy. As a result, gating for world-model precision and gating for attention are not explicitly differentiated in AIF, which identifies all of them with precision, whereas KT retains their conceptual separation.

4.4 Error Evaluation Dysfunctions

We next review how AD and psychedelic drugs (serotonergic hallucinogens) impact predictive coding, focusing on changes in error signaling and oscillatory mechanisms (gamma power and CFC).

Prediction-error processing can be probed with paradigms like the *mismatch negativity* (MMN) and the P300 component in event-related potentials in EEG/MEG.[127–129] The MMN is an early (100–250 ms) response to oddball stimuli deviating from a regular pattern, reflecting pre-attentive detection of prediction violations. The P300 (particularly its P3a/P3b subcomponents) is a later (∼300 ms) positive deflection associated with conscious evaluation of novel or target events and "updating" of context.[130,131] A related "local-global" auditory paradigm distinguishes lower-level mismatches from higher-order pattern violations: a local MMN might be generated by any deviant tone, whereas a global P3-like response occurs only if an entire sequence violates an abstract rule (e.g., sequence pattern), requiring intact hierarchical predictions. Gamma oscillations and CFC are increasingly examined within these paradigms, as transient gamma bursts and theta-gamma couplings have been observed during deviance detection, linking oscillatory dynamics to the evaluation of prediction errors.

4.4.1 Serotonergic Psychedelics

Classic serotonergic psychedelics (e.g., LSD, psilocybin, DMT) perturb the brain's predictive coding by acting as 5-HT_{2A} receptor agonists, acutely altering perception, cognition, and self-awareness. According to the REBUS model ("Relaxed Beliefs Under Psychedelics"), psychedelics reduce the precision of high-level priors (beliefs) in the brain's hierarchy.[132] By pharmacologically modulating deep-layer cortical neurons encoding predictions, psychedelics "liberate" bottom-up information flow.[132] In Bayesian terms, they lower the relative precision of top-down expectations, allowing normally suppressed prediction errors to ascend and influence conscious experience. This can explain the sensory hypersensitivity, cognitive disorganization, and hallucinations observed under psychedelics: with weakened priors' precision, sensory fluctuations may be over-interpreted, producing divergent percepts. Mechanistically, 5-HT_{2A} receptors are densely expressed on layer V pyramidal cells, whose excitability increases upon psychedelic binding.[110] Biophysical modeling of EEG/MEG data in humans under psilocybin are consistent with an increase of deep pyramidal cell excitability (gain) of deep pyramidal cells,[104,110] tipping the usual balance of cortical circuitry. Because these deep layers typically generate top-down signals, their heightened excitability disrupts the processing of weighted prediction errors, aligning with an 'anarchic' brain state where incoming sensations are less constrained by prior belief.[132]

Psychedelics' relaxation of top-down constraints also manifests in oscillatory changes, notably a broadband desynchronization of cortical rhythms. MEG and EEG studies show reduced power across the frequency spectrum under psilocybin and LSD (cortical power is reduced from delta through high gamma ranges in both frontal and posterior cortices).[110] Large power decreases are especially prominent in high-level default-mode network hubs,[110] suggesting a breakdown of dominant rhythmic activity. Similarly, low doses of LSD cause a dose-dependent reduction

in EEG power across the delta, theta, alpha, beta, and gamma bands during rest.[133] This global desynchronization is thought to index an increase in neuronal entropy or disorder[132]—essentially, neurons firing in a less constrained manner. In terms of predictive coding, such desynchronization corresponds to a collapse of precise priors (organized oscillatory states) and a release of sensory processing from descending constraints. Gamma-band oscillations, in particular, become abnormal. The reduction of alpha oscillations under psychedelics (alpha is dramatically reduced by psilocybin, and LSD[134]) likely contributes to this: since cross-frequency coupling often involves alpha/beta phase gating gamma, the disruption of slower oscillations means gamma activity is no longer properly coordinated in time. We can infer that the alpha-gamma and theta-gamma coupling that orchestrates hierarchical processing is weakened, and with it, an increase in the influence of sensory prediction errors.

Empirical evidence from prediction error paradigms under psychedelics underscores these changes. Using an auditory roving oddball (which assesses how MMN amplitude builds up with repeated standard stimuli), psilocybin was found to leave early error signaling largely intact: in one study, psilocybin did not significantly disrupt the MMN "memory trace" effect, whereas NMDA receptor blockade (ketamine) severely attenuated it.[131] This suggests that pre-attentive error detection in the sensory cortex (which relies on short-term synaptic plasticity and local circuit NMDA function) is not abolished by 5-HT_{2A} agonism—consistent with the idea that psychedelics primarily affect higher-level inference rather than basic sensory change detection. In contrast, at the level of conscious processing, psychedelics do have notable effects. The P300 response is reliably dampened by psychedelics. Under LSD, for instance, target oddball stimuli evoke a much smaller P300 amplitude compared to placebo.[133] This reduction of P300 (and prolongation of its latency) implies that the brain's ability to consciously evaluate and categorize events is impaired—likely because imprecise priors make it hard to decide what is contextually relevant. In a tactile mismatch paradigm, psilocybin likewise reduced the neural responses to surprising stimuli (both in EEG and associated fMRI activity in frontal and sensory regions), indicating aberrant error processing in multi-sensory domains.[135] Notably, some studies report that while "bottom-up" signals (like the basic MMN) remain, the later, more "top-down" components are disrupted.[135] This fits a picture in which psychedelics leave automatic error generation largely unimpeded or even enhanced but interfere with the brain's precision-weighting and integration of these errors into a coherent narrative.

In previous work,[104] we employed the LaNMM to explore the effects of serotonergic psychedelics. Using multi-modal neuroimaging data from thirty subjects diagnosed with Alzheimer's disease, we simulated the impact of serotonin 2A receptor activation on cortical dynamics. By modulating the excitability of layer 5 pyramidal neurons, our model reproduced the characteristic changes in EEG power spectra observed under psychedelics, including alpha power suppression and gamma power enhancement. These spectral shifts were shown to correlate strongly with the regional distribution of serotonin 2A receptors. Furthermore, simulated EEG revealed increased complexity and entropy, suggesting restored network function.

The present work expands on this research using the LaNMM to connect pathology with information-processing (cognitive) disruptions in the brain. Our results indicate that sero-

tonergic psychedelics weaken the influence of priors and precision attenuation mechanisms on error computation, leading to increased (precision-weighted) error signals even when the prior matches the input. The reduced influence of top-down precision-modulation signals suggests that, under psychedelics, the error signal primarily reflects the input itself rather than the mismatch between input and prior, effectively suppressing the prior's influence. This computational shift could explain psychedelic-induced perceptual distortions, where sensory signals are experienced with reduced interpretative constraints, as proposed by the REBUS model.[132] By disrupting hierarchical inference in this way, psychedelics may both destabilize perception and facilitate the revision of rigid priors, providing insight into their potential therapeutic effects.

4.4.2 PV+ Interneuron Dysfunction in Alzheimer's, Schizophrenia, and ASD

PV+ interneurons serve as a fundamental element of cortical circuit dynamics, enabling the tight inhibitory control and rhythmic synchronization necessary for normal cognition. In schizophrenia and ASD, disturbances in PV+ cell function and the resultant gamma oscillation impairments represent a common mechanistic thread, even as the clinical manifestations diverge. These impairments derail the brain's ability to engage in predictive coding – the efficient comparison of expectations and sensory inputs.

Alzheimer's disease is characterized by widespread cognitive deficits, which can be reinterpreted as resulting from aberrant predictive coding in neural networks.[130,136] Patients display blunted neural responses to unexpected stimuli across modalities. The subjective experience of AD begins in the preclinical phase with Subjective Cognitive Decline (SCD). SCD refers to self-reported experiences of worsening cognitive function without objective evidence of impairment on standard tests.[137] It is often one of the earliest noticeable symptoms in the AD continuum, preceding mild cognitive impairment and dementia. These subjective phenomena could be associated with an increased flow of prediction errors, as our model suggests.

In the clinical phase of AD, the auditory MMN is significantly reduced compared to healthy aging.[130] This attenuation of MMN is especially pronounced at longer inter-stimulus intervals, suggesting a rapid decay of the "memory trace" for standard stimuli—i.e. an impaired ability to maintain predictions over time. Even individuals at risk for AD (e.g., APOE4 carriers) show smaller MMNs than controls before clinical symptoms emerge.[130] AD also impairs the detection of higher-order regularities; for example, patients show deficits in perceiving melodic contour violations (sequence patterns in music),[130] indicating trouble with global predictive inferences. At a later processing stage, the P300 component is delayed and diminished in AD. Numerous studies and meta-analyses have found prolonged P300 latency and reduced amplitude in AD patients, correlating with cognitive decline.[131,133] The P3a (novelty-evoked) and P3b (target-evoked) subcomponents are often both affected, reflecting deficits in involuntary attention switching and conscious context updating, respectively. Overall, these ERP biomarkers suggest that AD brains generate weaker prediction errors and/or fail to effectively propagate them to higher levels for conscious detection. In a "global-local" auditory paradigm, one would predict that AD patients might detect simple local oddball deviations (driven by residual bottom-up signals) but struggle with global rule violations that require intact top-down integration—consistent with

findings that early sensory deviances are relatively preserved longer than complex cognitive prediction error in AD.[130]

AD is accompanied by marked changes in brain oscillatory activity. EEG shows a slowing of the background rhythm, with increased power in delta and theta bands and a loss of power in faster alpha, beta, and gamma frequencies.[138] Gamma oscillations, which depend on tightly synchronized inhibitory interneuron networks, are often impaired in AD. In animal models, interneuron dysfunction leads to deficits in gamma rhythmicity and aberrant network hyper-synchrony (e.g., epileptiform activity).[139] For instance, AD model mice with reduced GABAergic interneuron function show diminished gamma-band power and an over-synchronization of slower network activity. In humans, MEG/EEG studies have also reported reduced gamma responses during cognitive, sensory tasks or under evoked potentials induced by brain stimulation,[140] suggesting a compromised ability to generate the high-frequency activity associated with error signaling. Importantly, AD affects not only individual frequency bands but also their interactions.[138] Such alterations suggest that the normal hierarchical timing of predictions and errors is disrupted. GABAergic dysfunction is a key factor: postmortem and *in-vivo* studies indicate reduced cortical GABA levels and interneuron loss in AD.[141]

In previous work,[111] we used the LaNMM to represent the gradual dysfunction of PV interneurons due to Amyloid Beta oligomer toxicity and the subsequent loss of excitatory pyramidal neurons associated with advancing tau pathology. These mechanisms allowed our model to reproduce the full spectrum of AD electrophysiological biomarkers across disease development: early hyper-excitability—manifested as increased alpha synchrony and transient gamma enhancement—in preclinical and mild cognitive impairment stages, and later hypo-activation—characterized by a dominance of slow-wave (delta/theta) activity and diminished alpha/gamma power—in moderate-to-severe AD. Model outputs closely matched MEG/EEG findings across disease stages, supporting the hypothesis that fast interneuron dysfunction is the primary driver of AD's complex oscillatory dynamics.

Here, we extended this work by connecting the pathology in AD with information processing dysfunction, demonstrating how predictive coding mechanisms are progressively impaired as the disease advances. Our results indicate that the alterations in PV interneuron function lead to disruptions in both SEC and EEC mechanisms, affecting the brain's ability to suppress and compute prediction errors. In the MCI stage, the increased alpha and gamma power contribute to heightened error signals, reflecting an overactive yet unstable predictive system. In the AD stage, the overall power decrease—particularly in high-frequency bands—reduces the ability of the system to generate reliable prediction errors, leading to a collapse of error-signaling and comparator functionality. This is evident in the SEC scenario, where error suppression appears to recover in AD but is actually a byproduct of overall power loss rather than accurate predictive coding (Figure 12c). The disruption of error computation is further highlighted by the reduced influence of precision-modulating signals, revealing a severe breakdown of gating mechanisms in both MCI and AD stages. Notably, the largest disruptions are observed in MCI, consistent with the idea that interneuron dysfunction and alpha/gamma hyperactivity initially drive pathological changes before leading to widespread network collapse.

Finally, our model of PV+ dysfunction[111] is relevant to other conditions, such as ASD and schizophrenia, which also display information processing alterations such as sensory attenuation.[142–144] Interneuron dysfunction, particularly involving fast-spiking PV+ interneurons, is implicated in autism spectrum disorder (ASD),[145] Attention Deficit Hyperactive Disorder (ADHD,[146,147] and Schizophrenia.[148] In ASD, the number of PV+ cells is decreased across several cortical areas. Changes in the morphology or function of PV+ interneurons have also been linked to schizophrenia, epilepsy, and bipolar disorder.[149]

In schizophrenia, disrupted PV+ interneuron function leads to disrupted gamma oscillations,[149] impairing sensory processing and predictive coding. Similarly, in ASD, alterations in PV interneurons contribute to excitatory/inhibitory imbalances, affecting neural oscillations and predictive coding. These findings suggest that fast-spiking interneuron dysfunction across these disorders compromises neural oscillations and leads to cognitive deficits associated to predictive error evaluation disruptions.[150–152,152]

In summary, the LaNMM improves upon prior models by unifying multi-band oscillatory dynamics with weighted prediction-error computation in one coherent system. This advancement highlights the model's key contribution: a single model that simultaneously captures prediction, error, and their cross-frequency interactions, providing a clearer and more accurate account of cortical predictive processing.

4.5 Previous Computational Models of CFC and Prediction Error

Several physiologically grounded neural mass and network models have been developed to reproduce CFC phenomena such as PAC and AAC. For instance, Mejias et al. (2016)[153] introduced a laminar cortical network model of the primate visual hierarchy that captures distinct frequency-specific feedforward vs. feedback signaling. Slow oscillatory input from deep layers modulated superficial gamma, yielding PAC between layer-5/6 alpha (∼10 Hz) and layer-2/3 gamma (30–70 Hz). At the mesoscopic scale, NMMs with realistic neuronal interactions can intrinsically generate PAC. Chehelcheraghi et al. (2016)[154] adapted a cortical column model with pyramidal cells and fast and slow inhibitory interneurons. Under noise, the fast inhibitory subpopulation became a self-oscillatory gamma source, while the slow inhibitory rhythm in the alpha–theta range modulated the gamma amplitude, producing robust PAC. Extensions of this model also demonstrated other coupling types (phase–frequency, amplitude–amplitude, frequency–frequency). Sotero (2016)[155] highlighted how connectivity structure in a cortical column NMM shapes PAC generation, with balanced excitation–inhibition and resonant synapses modulating cross-frequency interactions. More recently, "next-generation" NMMs[156,157] replicated canonical CFC phenomena in coupled oscillatory circuits, attributing PAC emergence to interacting inhibitory populations or slow sinusoidal drives near a Hopf bifurcation. At the spiking-neuron level, models have also captured CFC with explicit physiological mappings.[158] Meanwhile, thalamocortical models showed how cortical slow oscillations (∼1 Hz) modulate thalamic sleep spindles (12–15 Hz), again reflecting phase-amplitude relationships.[159]

In parallel, some computational models explicitly encode prediction errors within physiologically grounded architectures. Rao and Ballard[115] proposed a hierarchical visual model where higher-

level feedback suppresses predicted inputs, forwarding only the residual unexplained signal. Spratling's cortical models[160] similarly use inhibitory feedback for residual error computation, and a network by Wacongne et al.[161] reproduces mismatch negativity by comparing predicted vs. actual tones. Canonical microcircuit models further propose that distinct cortical populations encode predictions vs. errors (deep vs. superficial layers), though details of how the error is evaluated remain less explicit.[162] Song et al.[163] extended these ideas to a pain perception NMM in which top–down analgesic expectations modulate incoming nociceptive signals, generating a residual error that drives cortical responses.

Though these studies illustrate how either CFC or explicit prediction error signals can be implemented, most do not address how cross-frequency interactions themselves underwrite prediction errors. In contrast, our approach incorporates both the generation of CFC and its computational role. By leveraging SEC and EEC, the proposed LaNMM provides a physiologically grounded instantiation of the Comparator function central to predictive coding frameworks. Unlike prior models that rely on noise-driven dynamics or impose CFC via structural constraints, the LaNMM produces emergent error signals approximating the difference between bottom-up sensory inputs (fast oscillatory envelopes) and top-down predictions (slower oscillations). This biologically plausible mechanism enables the dynamic, hierarchical modulation of prediction errors across multiple timescales. Furthermore, by integrating physiological constraints on laminar-specific processing, the LaNMM offers a unifying framework for studying predictive coding across cortical layers. In doing so, it builds a mechanistic bridge between abstract predictive coding theories and the neurophysiological generation of cross-frequency couplings, yielding new insights into both normal and pathological brain function.

4.6 Limitations

While our LaNMM approach captures key features of cross-frequency coupling and error evaluation, several limitations must be acknowledged. First, the model is an abstraction that simplifies complex cellular and synaptic dynamics; parameters were chosen based on theoretical and empirical considerations but may not fully capture the heterogeneous properties of real cortical networks.[3,4] Second, although our simulations reproduce oscillatory signatures observed in Alzheimer's disease and psychedelic states, such as altered gamma power and CFC patterns,[132,164] the direct translation of these findings to *in vivo* conditions requires further validation through combined EEG/MEG and invasive recordings. Third, the impact of neuromodulatory systems—especially the cholinergic and serotonergic influences—has been modeled in a simplified manner, and future work should integrate more detailed receptor-level dynamics to better account for state-dependent changes in error signaling. Fourth, our analysis covers only mesoscopic processing in single node dynamics, while both micro and macro network effects are undoubtedly relevant in predictive processing.

Finally, we have focused mainly here on the analysis of prediction error evaluation at the single column level and using a particular model displaying oscillations in the alpha and gamma bands. The model could be adjusted to other frequencies through parameter changes, and indeed, other models of oscillations exhibiting CFC could be used for the same purpose. Moreover,

the framework proposed can be extended across spatial and temporal scales. In particular, the information encoding scheme based on amplitude modulation can be extended hierarchically, with information encoded in signals, their envelopes, the envelopes of envelopes, etc.[100]

5 Conclusion

Our work supports the view that cross-frequency coupling provides a functional neural substrate for the evaluation of weighted prediction errors within a hierarchical predictive coding framework. The model presented here demonstrates how distinct modes of amplitude modulation—signal-envelope and envelope-envelope coupling—can instantiate a Comparator mechanism leveraging fast (gamma) and slow (alpha/beta) oscillatory dynamics. Moreover, the model speaks to causal relationships between neural CFC and cognitive functions[6] as well as a mechanistic perspective on how pathophysiology, such as n AD or induced by serotonergic psychedelics, disrupts the balance between top-down predictions and bottom-up error signaling.[110,130,132] Further work may explore the implications in other conditions associated with predictive coding abnormalities, such as schizophrenia,[150] ASD,[151] or ADHD.[152] Our mechanistic insights not only deepen our understanding of multiscale information processing in the brain but can guide the development of potential therapeutic interventions aimed at restoring normal oscillatory function and predictive coding.

References

[1] R P Rao and D H Ballard. Predictive coding in the visual cortex: a functional interpretation of some extra-classical receptive-field effects. *Nature Neuroscience*, 2(1):79–87, January 1999. Publisher: Springer Science and Business Media LLC.

[2] Karl Friston and Stefan Kiebel. Predictive coding under the free-energy principle. 364:1211–1221, 2009. tex.date-added: 2021-01-25 10:56:48 +0100 tex.date-modified: 2021-01-25 10:56:48 +0100.

[3] Andre M. Bastos, W. Martin Usrey, Rick A. Adams, George R. Mangun, Pascal Fries, and Karl J. Friston. Canonical microcircuits for predictive coding. *Neuron*, 76(4):695, November 2012.

[4] G. Spyropoulos and others. Layer and rhythm specificity for predictive routing. *Proceedings of the National Academy of Sciences*, 117(49):31459–31469, 2020.

[5] György Buzsáki and Brendon O. Watson. Brain rhythms and neural syntax: implications for efficient coding of cognitive content and neuropsychiatric disease. *Dialogues in Clinical Neuroscience*, 14(4):345–367, December 2012.

[6] Alexandre Hyafil, Anne-Lise Giraud, Lorenzo Fontolan, and Boris Gutkin. Neural Cross-Frequency Coupling: Connecting Architectures, Mechanisms, and Functions. *Trends in Neurosciences*, 38(11):725–740, November 2015.

[7] D. A. Pinotsis, N. Brunet, A. Bastos, C. A. Bosman, V. Litvak, P. Fries, and K. J. Friston. Contrast gain control and horizontal interactions in V1: a DCM study. *NeuroImage*, 92(100):143–155, May 2014.

[8] Stewart Shipp. Neural Elements for Predictive Coding. *Frontiers in Psychology*, 7, November 2016. Publisher: Frontiers.

[9] Karl Friston, James Kilner, and Lee Harrison. A free energy principle for the brain. *Journal of Physiology Paris*, 2006. Publisher: Elsevier tex.date-added: 2021-01-25 10:56:48 +0100 tex.date-modified: 2021-01-25 10:56:48 +0100.

[10] Thomas Parr. *Active inference : the free energy principle in mind, brain, and behavior*. The MIT Press, Cambridge, Massachusetts, 2022.

[11] Giulio Ruffini. Information, complexity, brains and reality ("Kolmogorov Manifesto"). *arXiv*, 2007. tex.date-added: 2009-03-01 11:09:48 +0100 tex.date-modified: 2009-06-06 18:41:44 +0200.

[12] Giulio Ruffini. Reality as Simplicity, June 2009. arXiv:0903.1193 [physics].

[13] Giulio Ruffini. Models, networks and algorithmic complexity. *arxiv*, 2016. Publisher: arXiv.

[14] Giulio Ruffini. An algorithmic information theory of consciousness. *Neuroscience of Consciousness*, 2017(1):nix019, 2017.

[15] Giulio Ruffini and Edmundo Lopez-Sola. AIT foundations of structured experience. *Journal of Artificial Intelligence and Consciousness*, 9(2):153–191, September 2022. Publisher: World Scientific Pub Co Pte Ltd.

[16] Giulio Ruffini, Francesca Castaldo, Edmundo Lopez-Sola, Roser Sanchez-Todo, and Jakub Vohryzek. The Algorithmic Agent Perspective and Computational Neuropsychiatry: From Etiology to Advanced Therapy in Major Depressive Disorder. *Entropy*, 26(11):953, November 2024. Number: 11 Publisher: Multidisciplinary Digital Publishing Institute.

[17] Giulio Ruffini, Francesca Castaldo, and Jakub Vohryzek. Structured Dynamics in the Algorithmic Agent. *Entropy*, 27(1):90, January 2025. Number: 1 Publisher: Multidisciplinary Digital Publishing Institute.

[18] Thomas M. Cover and Joy A. Thomas. *Elements of information theory*. John Wiley & sons, 2 edition, 2006. tex.date-added: 2016-10-20 21:00:29 +0000 tex.date-modified: 2016-10-20 21:00:58 +0000.

[19] Karl Friston. Hierarchical models in the brain. *PLoS computational biology*, 4(11):e1000211, November 2008.

[20] Ole Jensen and Ali Mazaheri. Shaping Functional Architecture by Oscillatory Alpha Activity: Gating by Inhibition. *Frontiers in Human Neuroscience*, 4:186, November 2010.

[21] André M Bastos, Mikael Lundqvist, Ayan S Waite, Nancy Kopell, and Earl K Miller. Layer and rhythm specificity for predictive routing. *Proceedings of the National Academy of*

Sciences of the United States of America, 117(49):31459–31469, December 2020. Publisher: Proceedings of the National Academy of Sciences.

[22] Pascal Fries. A mechanism for cognitive dynamics: neuronal communication through neuronal coherence. *Trends in Cognitive Sciences*, 9(10):474–480, October 2005.

[23] André Moraes Bastos, Julien Vezoli, Conrado Arturo Bosman, Jan-Mathijs Schoffelen, Robert Oostenveld, Jarrod Robert Dowdall, Peter De Weerd, Henry Kennedy, and Pascal Fries. Visual areas exert feedforward and feedback influences through distinct frequency channels. *Neuron*, 85(2):390–401, January 2015.

[24] Thilo Womelsdorf, Jan-Mathijs Schoffelen, Robert Oostenveld, Wolf Singer, Robert Desimone, Andreas K. Engel, and Pascal Fries. Modulation of neuronal interactions through neuronal synchronization. *Science (New York, N.Y.)*, 316(5831):1609–1612, June 2007.

[25] Pascal Fries. Neuronal gamma-band synchronization as a fundamental process in cortical computation. *Annual Review of Neuroscience*, 32:209–224, 2009.

[26] Christini Katsanevaki, André M. Bastos, Hayriye Cagnan, Conrado A. Bosman, Karl J. Friston, and Pascal Fries. Attentional effects on local V1 microcircuits explain selective V1-V4 communication. *NeuroImage*, 281:120375, November 2023.

[27] R. E. Kalman. A New Approach to Linear Filtering and Prediction Problems. *Journal of Basic Engineering*, 82(1):35–45, March 1960.

[28] György Buzsáki and Xiao-Jing Wang. Mechanisms of gamma oscillations. *Annual Review of Neuroscience*, 35:203–225, 2012.

[29] M. A. Whittington, R. D. Traub, N. Kopell, B. Ermentrout, and E. H. Buhl. Inhibition-based rhythms: experimental and mathematical observations on network dynamics. *International Journal of Psychophysiology: Official Journal of the International Organization of Psychophysiology*, 38(3):315–336, December 2000.

[30] Ole Jensen, Jochen Kaiser, and Jean-Philippe Lachaux. Human gamma-frequency oscillations associated with attention and memory. *Trends in Neurosciences*, 30(7):317–324, July 2007.

[31] Magdalena Nowak, Catharina Zich, and Charlotte J. Stagg. Motor Cortical Gamma Oscillations: What Have We Learnt and Where Are We Headed? *Current Behavioral Neuroscience Reports*, 5(2):136–142, 2018.

[32] Erika Nyhus and Tim Curran. Functional role of gamma and theta oscillations in episodic memory. *Neuroscience and Biobehavioral Reviews*, 34(7):1023–1035, June 2010.

[33] Yong-Wook Shin, Brian F. O'Donnell, Soyoung Youn, and Jun Soo Kwon. Gamma Oscillation in Schizophrenia. *Psychiatry Investigation*, 8(4):288, December 2011.

[34] Ao Guan, Shaoshuang Wang, Ailing Huang, Chenyue Qiu, Yansong Li, Xuying Li, Jinfei Wang, Qiang Wang, and Bin Deng. The role of gamma oscillations in central nervous sys-

tem diseases: Mechanism and treatment. *Frontiers in Cellular Neuroscience*, 16:962957, 2022.

[35] Valerio Manippa, Annalisa Palmisano, Marco Filardi, Davide Vilella, Michael A. Nitsche, Davide Rivolta, and Giancarlo Logroscino. An update on the use of gamma (multi)sensory stimulation for Alzheimer's disease treatment. *Frontiers in Aging Neuroscience*, 14:1095081, 2022.

[36] Tallan Black, Bryan W. Jenkins, Robert B. Laprairie, and John G. Howland. Therapeutic potential of gamma entrainment using sensory stimulation for cognitive symptoms associated with schizophrenia. *Neuroscience & Biobehavioral Reviews*, 161:105681, June 2024.

[37] W. Singer and C. M. Gray. Visual feature integration and the temporal correlation hypothesis. *Annual Review of Neuroscience*, 18:555–586, 1995.

[38] Connor G. Gallimore, David A. Ricci, and Jordan P. Hamm. Spatiotemporal dynamics across visual cortical laminae support a predictive coding framework for interpreting mismatch responses. *Cerebral Cortex (New York, NY)*, 33(15):9417, June 2023.

[39] Conrado A. Bosman, Carien S. Lansink, and Cyriel M. A. Pennartz. Functions of gamma-band synchronization in cognition: from single circuits to functional diversity across cortical and subcortical systems. *The European Journal of Neuroscience*, 39(11):1982–1999, June 2014.

[40] Wolfgang Klimesch, Paul Sauseng, and Simon Hanslmayr. EEG alpha oscillations: the inhibition-timing hypothesis. *Brain Research Reviews*, 53(1):63–88, January 2007.

[41] Simon Hanslmayr, Joachim Gross, Wolfgang Klimesch, and Kimron L. Shapiro. The role of alpha oscillations in temporal attention. *Brain Research Reviews*, 67(1-2):331–343, June 2011.

[42] W. Klimesch. EEG alpha and theta oscillations reflect cognitive and memory performance: a review and analysis. *Brain Research. Brain Research Reviews*, 29(2-3):169–195, April 1999.

[43] Per B. Sederberg, Michael J. Kahana, Marc W. Howard, Elizabeth J. Donner, and Joseph R. Madsen. Theta and Gamma Oscillations during Encoding Predict Subsequent Recall. *The Journal of Neuroscience*, 23(34):10809, November 2003.

[44] Bradley Voytek, Ryan T. Canolty, Avgusta Shestyuk, Nathan E. Crone, Josef Parvizi, and Robert T. Knight. Shifts in Gamma Phase–Amplitude Coupling Frequency from Theta to Alpha Over Posterior Cortex During Visual Tasks. *Frontiers in Human Neuroscience*, 4:191, October 2010.

[45] Timo van Kerkoerle, Matthew W. Self, Bruno Dagnino, Marie-Alice Gariel-Mathis, Jasper Poort, Chris van der Togt, and Pieter R. Roelfsema. Alpha and gamma oscillations characterize feedback and feedforward processing in monkey visual cortex. *Proceedings*

of the National Academy of Sciences of the United States of America, 111(40):14332, September 2014.

[46] Dorottya Hetenyi, Joost Haarsma, and Peter Kok. Pre-stimulus alpha oscillations encode stimulus-specific visual predictions, March 2024. Pages: 2024.03.13.584593 Section: New Results.

[47] William Turner, Tessel Blom, and Hinze Hogendoorn. Visual Information Is Predictively Encoded in Occipital Alpha/Low-Beta Oscillations. *The Journal of Neuroscience*, 43(30):5537–5545, July 2023.

[48] Anna Mayer, Caspar M. Schwiedrzik, Michael Wibral, Wolf Singer, and Lucia Melloni. Expecting to See a Letter: Alpha Oscillations as Carriers of Top-Down Sensory Predictions. *Cerebral Cortex*, 26(7):3146–3160, July 2016.

[49] Malte Wöstmann, Mohsen Alavash, and Jonas Obleser. Alpha Oscillations in the Human Brain Implement Distractor Suppression Independent of Target Selection. *Journal of Neuroscience*, 39(49):9797–9805, December 2019. Publisher: Society for Neuroscience Section: Research Articles.

[50] György Buzsáki. *Rhythms of the brain.* Oxford University Press, Oxford New York, 2006.

[51] John E. Lisman and Ole Jensen. The Theta-Gamma Neural Code. *Neuron*, 77(6):1002–1016, March 2013.

[52] Robson Scheffer-Teixeira and Adriano Bl Tort. On cross-frequency phase-phase coupling between theta and gamma oscillations in the hippocampus. *eLife*, 5:e20515, December 2016.

[53] Anne-Lise Giraud and David Poeppel. Cortical oscillations and speech processing: emerging computational principles and operations. *Nature Neuroscience*, 15(4):511–517, April 2012. Publisher: Nature Publishing Group.

[54] Nai Ding and Jonathan Z. Simon. Neural coding of continuous speech in auditory cortex during monaural and dichotic listening. *Journal of Neurophysiology*, 107(1):78–89, January 2012.

[55] James A. O'Sullivan, Alan J. Power, Nima Mesgarani, Siddharth Rajaram, John J. Foxe, Barbara G. Shinn-Cunningham, Malcolm Slaney, Shihab A. Shamma, and Edmund C. Lalor. Attentional Selection in a Cocktail Party Environment Can Be Decoded from Single-Trial EEG. *Cerebral Cortex (New York, N.Y.: 1991)*, 25(7):1697–1706, July 2015.

[56] Nima Mesgarani and Edward F. Chang. Selective cortical representation of attended speaker in multi-talker speech perception. *Nature*, 485(7397):10.1038/nature11020, May 2012.

[57] Elana M. Zion Golumbic, Nai Ding, Stephan Bickel, Peter Lakatos, Catherine A. Schevon, Guy M. McKhann, Robert R. Goodman, Ronald Emerson, Ashesh D. Mehta, Jonathan Z.

Simon, David Poeppel, and Charles E. Schroeder. Mechanisms Underlying Selective Neuronal Tracking of Attended Speech at a 'Cocktail Party'. *Neuron*, 77(5):980, March 2013.

[58] Vibha Viswanathan, Hari M. Bharadwaj, and Barbara G. Shinn-Cunningham. Electroencephalographic Signatures of the Neural Representation of Speech during Selective Attention. *eNeuro*, 6(5), September 2019. Publisher: Society for Neuroscience Section: New Research.

[59] Raphael Kaplan, Daniel Bush, Mathilde Bonnefond, Peter A. Bandettini, Gareth R. Barnes, Christian F. Doeller, and Neil Burgess. Medial prefrontal theta phase coupling during spatial memory retrieval. *Hippocampus*, 24(6):656–665, June 2014.

[60] Pascal Fries. Rhythms for Cognition: Communication through Coherence. *Neuron*, 88(1):220–235, October 2015.

[61] Tisa Hodnik, Stiven Roytman, Nico I. Bohnen, and Uros Marusic. Beta–Gamma Phase-Amplitude Coupling as a Non-Invasive Biomarker for Parkinson's Disease: Insights from Electroencephalography Studies. *Life*, 14(3):391, March 2024.

[62] Andrew B. O'Keeffe, Mahsa Malekmohammadi, Hiro Sparks, and Nader Pouratian. Synchrony Drives Motor Cortex Beta Bursting, Waveform Dynamics, and Phase-Amplitude Coupling in Parkinson's Disease. *The Journal of Neuroscience: The Official Journal of the Society for Neuroscience*, 40(30):5833–5846, July 2020.

[63] Hong-Yuan Chu, Yoland Smith, William W. Lytton, Scott Grafton, Rosa Villalba, Gunasingh Masilamoni, and Thomas Wichmann. Dysfunction of motor cortices in Parkinson's disease. *Cerebral Cortex (New York, NY)*, 34(7):bhae294, July 2024.

[64] Annaelle Devergnas, Damien Pittard, Donald Bliwise, and Thomas Wichmann. Relationship between oscillatory activity in the cortico-basal ganglia network and parkinsonism in MPTP-treated monkeys. *Neurobiology of Disease*, 68:156–166, August 2014.

[65] Roberto C. Sotero, Lazaro M. Sanchez-Rodriguez, Mehdy Dousty, Yasser Iturria-Medina, and Jose M. Sanchez-Bornot. Cross-Frequency Interactions During Information Flow in Complex Brain Networks Are Facilitated by Scale-Free Properties. *Frontiers in Physics*, 7:107, July 2019.

[66] Daniella B Victorino, Jean Faber, Daniel J. L. L Pinheiro, Fulvio A Scorza, Antônio C. G Almeida, Alberto C. S Costa, and Carla A Scorza. Toward the Identification of Neurophysiological Biomarkers for Alzheimer's Disease in Down Syndrome: A Potential Role for Cross-Frequency Phase-Amplitude Coupling Analysis. *Aging and Disease*, 14(2):428–449, April 2023.

[67] Pooja Prabhu, Hirofumi Morise, Kiwamu Kudo, Alexander Beagle, Danielle Mizuiri, Faatimah Syed, Karunakar A Kotegar, Anne Findlay, Bruce L Miller, Joel H Kramer, Katherine P Rankin, Paul A Garcia, Heidi E Kirsch, Keith Vossel, Srikantan S Nagarajan, and Kamalini G Ranasinghe. Abnormal gamma phase-amplitude coupling in the parahip-

pocampal cortex is associated with network hyperexcitability in Alzheimer's disease. *Brain Communications*, 6(2):fcae121, April 2024.

[68] Jesus Poza, Alejandro Bachiller, Carlos Gomez, Maria Garcia, Pablo Nunez, Javier Gomez-Pilar, Miguel A. Tola-Arribas, Monica Cano, and Roberto Hornero. Phase-amplitude coupling analysis of spontaneous EEG activity in Alzheimer's disease. *Annual International Conference of the IEEE Engineering in Medicine and Biology Society. IEEE Engineering in Medicine and Biology Society. Annual International Conference*, 2017:2259–2262, July 2017.

[69] Paolo Bazzigaluppi, Tina L. Beckett, Margaret M. Koletar, Aaron Y. Lai, Illsung L. Joo, Mary E. Brown, Peter L. Carlen, JoAnne McLaurin, and Bojana Stefanovic. Early-stage attenuation of phase-amplitude coupling in the hippocampus and medial prefrontal cortex in a transgenic rat model of Alzheimer's disease. *Journal of Neurochemistry*, 144(5):669–679, March 2018.

[70] Hannah F. Iaccarino, Annabelle C. Singer, Anthony J. Martorell, Andrii Rudenko, Fan Gao, Tyler Z. Gillingham, Hansruedi Mathys, Jinsoo Seo, Oleg Kritskiy, Fatema Abdurrob, Chinnakkaruppan Adaikkan, Rebecca G. Canter, Richard Rueda, Emery N. Brown, Edward S. Boyden, and Li-Huei Tsai. Gamma frequency entrainment attenuates amyloid load and modifies microglia. *Nature*, 540(7632):230–235, December 2016.

[71] Anthony J. Martorell, Abigail L. Paulson, Ho-Jun Suk, Fatema Abdurrob, Gabrielle T. Drummond, Webster Guan, Jennie Z. Young, David Nam-Woo Kim, Oleg Kritskiy, Scarlett J. Barker, Vamsi Mangena, Stephanie M. Prince, Emery N. Brown, Kwanghun Chung, Edward S. Boyden, Annabelle C. Singer, and Li-Huei Tsai. Multi-sensory Gamma Stimulation Ameliorates Alzheimer's-Associated Pathology and Improves Cognition. *Cell*, 177(2):256–271.e22, April 2019.

[72] Giulia Sprugnoli, Fanny Munsch, Davide Cappon, Rachel Paciorek, Joanna Macone, Ann Connor, Georges El Fakhri, Ricardo Salvador, Giulio Ruffini, Kevin Donohoe, Mouhsin M. Shafi, Daniel Press, David C. Alsop, Alvaro Pascual Leone, and Emiliano Santarnecchi. Impact of multisession 40Hz tACS on hippocampal perfusion in patients with Alzheimer's disease. *Alzheimer's Research & Therapy*, 13(1):203, December 2021.

[73] Seyyedeh Nahaleh Fatemi, Mohammad Javad Sedghizadeh, and Hamid Aghajan. Theta-gamma phase-amplitude coupling explains the advantage of auditory plus visual gamma entrainment in Alzheimer's therapy. *Alzheimer's & Dementia*, 17(S7):e053451, 2021. _eprint: https://onlinelibrary.wiley.com/doi/pdf/10.1002/alz.053451.

[74] Shogo Hirano, Alexander Nakhnikian, Yoji Hirano, Naoya Oribe, Shigenobu Kanba, Toshiaki Onitsuka, Margaret Levin, and Kevin M. Spencer. Phase-Amplitude Coupling of the Electroencephalogram in the Auditory Cortex in Schizophrenia. *Biological Psychiatry. Cognitive Neuroscience and Neuroimaging*, 3(1):69–76, January 2018.

[75] Dashiell D. Sacks, Paul E. Schwenn, Larisa T. McLoughlin, Jim Lagopoulos, and Daniel F. Hermens. Phase–Amplitude Coupling, Mental Health and Cognition: Implications for Adolescence. *Frontiers in Human Neuroscience*, 15, March 2021. Publisher: Frontiers.

[76] Minah Kim, Yurim Shim, Junbeom Kwon, Sangyoon Bae, Junhee Lee, Jiook Cha, Soo-Hee Choi, Se Hyun Kim, Ung Gu Kang, and Jun Soo Kwon. Resting-state theta-phase gamma amplitude coupling as a biomarker for the transdiagnostic dimensional approach in psychiatric disorders. *Psychiatry and Clinical Neurosciences*, 77(7):410–411, July 2023.

[77] Brian H. Silverstein, Nicholas Kolbman, Amanda Nelson, Tiecheng Liu, Peter Guzzo, Jim Gilligan, UnCheol Lee, George A. Mashour, Giancarlo Vanini, and Dinesh Pal. Psilocybin induces dose-dependent changes in functional network organization in rat cortex. *bioRxiv: The Preprint Server for Biology*, page 2024.02.09.579718, February 2024.

[78] Gustavo Deco, Viktor K. Jirsa, Peter A. Robinson, Michael Breakspear, and Karl Friston. The Dynamic Brain: From Spiking Neurons to Neural Masses and Cortical Fields. *PLOS Computational Biology*, 4(8):e1000092, August 2008. Publisher: Public Library of Science.

[79] Michael Breakspear. Dynamic models of large-scale brain activity. *Nature Neuroscience*, 20(3):340–352, February 2017.

[80] Olaf Sporns, Giulio Tononi, and Rolf Kötter. The human connectome: A structural description of the human brain. *PLoS Comput. Biol.*, 1(4):e42, September 2005. Publisher: Public Library of Science (PLoS).

[81] Isabelle Merlet, Gwenael Birot, Ricardo Salvador, Behnam Molaee-Ardekani, Abeye Mekonnen, Aureli Soria-Frish, Giulio Ruffini, Pedro C. Miranda, and Fabrice Wendling. From oscillatory transcranial current stimulation to scalp EEG changes: A biophysical and physiological modeling study. *PLoS ONE*, 8(2):e57330, February 2013. tex.date-added: 2016-06-10 15:40:27 +0000 tex.date-modified: 2016-06-10 15:42:30 +0000.

[82] V. B. Mountcastle. The columnar organization of the neocortex. *Brain: A Journal of Neurology*, 120 (Pt 4):701–722, April 1997.

[83] B. H. Jansen and V. G. Rit. Electroencephalogram and visual evoked potential generation in a mathematical model of coupled cortical columns. *Biological Cybernetics*, 73(4):357–366, September 1995.

[84] François Grimbert and Olivier Faugeras. Bifurcation analysis of Jansen's neural mass model. *Neural Computation*, 18(12):3052–3068, December 2006.

[85] E. J. Doedel and others. AUTO-07P: Continuation and bifurcation software for ordinary differential equations. manual, 2007.

[86] Roser Sanchez-Todo, André M. Bastos, Edmundo Lopez-Sola, Borja Mercadal, Emiliano Santarnecchi, Earl K. Miller, Gustavo Deco, and Giulio Ruffini. A physical neural mass model framework for the analysis of oscillatory generators from laminar electrophysiological recordings. *NeuroImage*, 270:119938, April 2023.

[87] Giulio Ruffini, Edmundo Lopez-Sola, Jakub Vohryzek, and Roser Sanchez-Todo. Neural geometrodynamics, complexity, and plasticity: a psychedelics perspective. *Entropy*, 26(1):90, 2024. Publisher: MDPI.

[88] André M. Bastos, Roman Loonis, Simon Kornblith, Mikael Lundqvist, and Earl K. Miller. Laminar recordings in frontal cortex suggest distinct layers for maintenance and control of working memory. *Proceedings of the National Academy of Sciences*, 115(5):1117–1122, 2018.

[89] Diego Mendoza-Halliday, Alex James Major, Noah Lee, Maxwell J. Lichtenfeld, Brock Carlson, Blake Mitchell, Patrick D. Meng, Yihan (Sophy) Xiong, Jacob A. Westerberg, Xiaoxuan Jia, Kevin D. Johnston, Janahan Selvanayagam, Stefan Everling, Alexander Maier, Robert Desimone, Earl K. Miller, and André M. Bastos. A ubiquitous spectrolaminar motif of local field potential power across the primate cortex. *Nature Neuroscience*, pages 1–14, January 2024. Publisher: Nature Publishing Group.

[90] F. Wendling, F. Bartolomei, J. J. Bellanger, and P. Chauvel. Epileptic fast activity can be explained by a model of impaired GABAergic dendritic inhibition. *The European Journal of Neuroscience*, 15(9):1499–1508, May 2002.

[91] Mojtaba Chehelcheraghi, Chie Nakatani, Erik Steur, and Cees van Leeuwen. A neural mass model of phase–amplitude coupling. *Biological Cybernetics*, 110(2):171–192, June 2016.

[92] Mojtaba Chehelcheraghi, Cees van Leeuwen, Erik Steur, and Chie Nakatani. A neural mass model of cross frequency coupling. *PLOS ONE*, 12(4):e0173776, April 2017. Publisher: Public Library of Science.

[93] G. Ruffini, R. Sanchez-Todo, L. Dubreuil, R. Salvador, D. Pinotsis, E. K. Miller, F. Wendling, E. Santarnecchi, and A. Bastos. P118 A Biophysically realistic Laminar Neural Mass Modeling framework for transcranial Current Stimulation. *Clinical Neurophysiology*, 131(4):e78–e79, April 2020.

[94] Borja Mercadal, Edmundo Lopez-Sola, Adrià Galan-Gadea, Mariam Al Harrach, Roser Sanchez-Todo, Ricardo Salvador, Fabrice Bartolomei, Fabrice Wendling, and Giulio Ruffini. Towards a mesoscale physical modeling framework for stereotactic-EEG recordings. *Journal of Neural Engineering*, 20(1), January 2023.

[95] A. M. Bastos, V. Litvak, R. Moran, C. A. Bosman, P. Fries, and K. J. Friston. A DCM study of spectral asymmetries in feedforward and feedback connections between visual areas V1 and V4 in the monkey. *NeuroImage*, 108:460–475, March 2015.

[96] Karl J Friston, André M Bastos, Dimitris Pinotsis, and Vladimir Litvak. LFP and oscillations—what do they tell us? *Current Opinion in Neurobiology*, 31:1–6, April 2015.

[97] György Buzsáki and Andreas Draguhn. Neuronal oscillations in cortical networks. *Science (New York, N.Y.)*, 304(5679):1926–1929, June 2004.

[98] Shunsuke Tamura and Yoji Hirano. Cortical representation of speech temporal information through high gamma-band activity and its temporal modulation. *Cerebral Cortex (New York, NY)*, 33(13):8773, May 2023.

[99] Brian N. Pasley, Stephen V. David, Nima Mesgarani, Adeen Flinker, Shihab A. Shamma, Nathan E. Crone, Robert T. Knight, and Edward F. Chang. Reconstructing Speech from Human Auditory Cortex. *PLOS Biology*, 10(1):e1001251, January 2012. Publisher: Public Library of Science.

[100] Giulio Ruffini and Francesca Castaldo. Neural Encoding through Hiearchical Amplitude Modulation (HAM): a Laminar Neural Mass model implementation ("it is AM radio"). *biorxiv*, 2025.

[101] Ryota Kanai, Yutaka Komura, Stewart Shipp, and Karl Friston. Cerebral hierarchies: predictive processing, precision and the pulvinar. *Philosophical Transactions of the Royal Society of London. Series B, Biological Sciences*, 370(1668):20140169, May 2015.

[102] G Ruffini, R Sanchez-Todo, L Dubreuil, R Salvador, D Pitosis, Earl K Miller, F Wendling, E Santarnecchi, and A Bastos. A Biologically realistic Laminar Neural Mass Modeling Framework for Transcranial Electrical Stimulation. *Clinical Neurophysiology*, 131(4):e78–e79, 2020.

[103] Pau Clusella, Gustavo Deco, Morten L. Kringelbach, Giulio Ruffini, and Jordi Garcia-Ojalvo. Complex spatiotemporal oscillations emerge from transverse instabilities in large-scale brain networks. *PLOS Computational Biology*, 19(4):e1010781, April 2023. Publisher: Public Library of Science.

[104] Jan C. Gendra, Edmundo Lopez-Sola, Francesca Castaldo, Elia Lleal-Custey, Roser Sanchez-Todo, Jakub Vohryzek, Ricardo Salvador, and Giulio Ruffini. Restoring Oscillatory Dynamics in Alzheimer's Disease: A Laminar Whole-Brain Model of Serotonergic Psychedelic Effects, December 2024.

[105] Eelke Spaak, Mathilde Bonnefond, Alexander Maier, David A. Leopold, and Ole Jensen. Layer-specific entrainment of gamma-band neural activity by the alpha rhythm in monkey visual cortex. *Current biology : CB*, 22(24):2313, November 2012.

[106] Sara M. Szczepanski, Nathan E. Crone, Rachel A. Kuperman, Kurtis I. Auguste, Josef Parvizi, and Robert T. Knight. Dynamic changes in phase-amplitude coupling facilitate spatial attention control in fronto-parietal cortex. *PLoS biology*, 12(8):e1001936, August 2014.

[107] Dino Dvorak and André A. Fenton. Towards a proper estimation of phase-amplitude coupling in neural oscillations. *Journal of neuroscience methods*, 225:42, January 2014.

[108] Jorge F. Mejias, John D. Murray, Henry Kennedy, and Xiao-Jing Wang. Feedforward and feedback frequency-dependent interactions in a large-scale laminar network of the primate cortex. *Science Advances*, 2(11):e1601335, November 2016.

[109] Ravi V. Chacko, Byungchan Kim, Suh Woo Jung, Amy L. Daitch, Jarod L. Roland, Nicholas V. Metcalf, Maurizio Corbetta, Gordon L. Shulman, and Eric C. Leuthardt. Distinct phase-amplitude couplings distinguish cognitive processes in human attention. *NeuroImage*, 175:111–121, July 2018.

[110] Suresh D. Muthukumaraswamy, Robin L. Carhart-Harris, Rosalyn J. Moran, Matthew J. Brookes, Tim M. Williams, David Errtizoe, Ben Sessa, Andreas Papadopoulos, Mark Bolstridge, Krish D. Singh, Amanda Feilding, Karl J. Friston, and David J. Nutt. Broadband Cortical Desynchronization Underlies the Human Psychedelic State. *Journal of Neuroscience*, 33(38):15171–15183, September 2013. Publisher: Society for Neuroscience Section: Articles.

[111] Roser Sanchez-Todo, Lopez-Sola Edmundo, Mercadal Borja, and Ruffini Giulio. Laminar Neural Mass Model for Representing Alzheimer's Disease Electrophysiopathology. *biorxiv*, 2024.

[112] Peter Cariani and Janet M. Baker. Time Is of the Essence: Neural Codes, Synchronies, Oscillations, Architectures. *Frontiers in Computational Neuroscience*, 16:898829, 2022.

[113] Ian G. Cumming and Frank H. Wong. *Digital Processing of Synthetic Aperture Radar Data: Algorithms and Implementation.* Artech House, Boston, MA, USA, 2005.

[114] P. Elias. Predictive coding–I. *IRE Transactions on Information Theory*, 1(1):16–24, 1955.

[115] Rajesh P. N. Rao and Dana H. Ballard. Predictive coding in the visual cortex: a functional interpretation of some extra-classical receptive-field effects. *Nature Neuroscience*, 2(1):79–87, 1999.

[116] M. V. Srinivasan, S. B. Laughlin, and A. Dubs. Predictive coding: a fresh view of inhibition in the retina. *Proceedings of the Royal Society of London. Series B, Biological Sciences*, 216(1205):427–459, November 1982.

[117] W. Ross Ashby. *An Introduction to Cybernetics.* Martino Fine Books, 2015.

[118] Alan M. Turing. On computable numbers, with an application to the entscheidungsproblem. *Proceedings of the London Mathematical Society*, 2(42):230–265, 1936. tex.date-added: 2016-12-21 19:54:54 +0000 tex.date-modified: 2016-12-22 00:59:02 +0000.

[119] Paul Bernays. Alonzo Church. An unsolvable problem of elementary number theory. American journal of mathematics, vol. 58 (1936), pp. 345–363. *The Journal of Symbolic Logic*, 1(2):73–74, June 1936.

[120] C. E. Shannon. A mathematical theory of communication. *The Bell System Technical Journal*, 27(3):379–423, July 1948. Conference Name: The Bell System Technical Journal.

[121] Richard P. Feynman. *Feynman lectures on computation.* Advanced book program. Perseus, Cambridge, Mass, paperback print., [repr.] edition, 2001.

[122] Doron Swade. *The Difference Engine: Charles Babbage and the Quest to Build the First Computer.* Penguin, 2000.

[123] Brian Jack Copeland, editor. *Colossus: the secrets of Bletchley Park's codebreaking computers*. Oxford University Press, Oxford New York, 2006.

[124] Brian Randell. On alan turing and the origins of digital computers. In B. Meltzer and D. Michie, editors, *Machine Intelligence*, volume 7, pages 3–20. 1972.

[125] Jeffry S. Isaacson and Massimo Scanziani. How inhibition shapes cortical activity. *Neuron*, 72(2):231–243, 2011.

[126] Ashish Vaswani, Noam Shazeer, Niki Parmar, Jakob Uszkoreit, Llion Jones, Aidan N. Gomez, Łukasz Kaiser, and Illia Polosukhin. Attention is all you need. In *Proceedings of the 31st International Conference on Neural Information Processing Systems*, NIPS'17, pages 6000–6010, Red Hook, NY, USA, December 2017. Curran Associates Inc.

[127] R. Näätänen, M. Tervaniemi, E. Sussman, P. Paavilainen, and I. Winkler. "Primitive intelligence" in the auditory cortex. *Trends in Neurosciences*, 24(5):283–288, May 2001.

[128] Marta I. Garrido, James M. Kilner, Klaas E. Stephan, and Karl J. Friston. The mismatch negativity: A review of underlying mechanisms. *Clinical Neurophysiology*, 120(3):453–463, March 2009.

[129] Brendon Qela, Stefano Damiani, Samanta De Santis, Federica Groppi, Anna Pichiecchio, Carlo Asteggiano, Natascia Brondino, Alessio Maria Monteleone, Luigi Grassi, Pierluigi Politi, Paolo Fusar-Poli, and Laura Fusar-Poli. Predictive coding in neuropsychiatric disorders: A systematic transdiagnostic review. *Neuroscience & Biobehavioral Reviews*, 169:106020, February 2025.

[130] E. Pekkonen. Mismatch negativity in aging and in Alzheimer's and Parkinson's diseases. *Audiology and Neurotology*, 5(3-4):216–224, 2000.

[131] André Schmidt, Rosilla Bachmann, Michael Kometer, Philipp A. Csomor, Klaas E. Stephan, Erich Seifritz, and Franz X. Vollenweider. Mismatch negativity encoding of prediction errors predicts S-ketamine-induced cognitive impairments. *Neuropsychopharmacology: Official Publication of the American College of Neuropsychopharmacology*, 37(4):865–875, March 2012.

[132] R L Carhart-Harris and K J Friston. REBUS and the anarchic brain: Toward a unified model of the brain action of psychedelics. *Pharmacological Reviews*, 71(3):316–344, July 2019. Publisher: American Society for Pharmacology & Experimental Therapeutics (ASPET).

[133] Conor H. Murray, Ilaria Tare, Claire M. Perry, Michael Malina, Royce Lee, and Harriet de Wit. Low doses of LSD reduce broadband oscillatory power and modulate event-related potentials in healthy adults. *Psychopharmacology*, 239(6):1735–1747, June 2022.

[134] M. Kometer and others. Psilocybin biases facial recognition, reduces negative affect, and enhances bonding: behavioral and neural effects. *Biological Psychiatry*, 73(8):731–738, 2013.

[135] C. Pallavicini and others. Psilocybin-induced modulation of EEG and fMRI signals during a tactile learning task: evidence for aberrant prediction error processing. *Cerebral Cortex*, 32(1):186–204, 2021.

[136] Ece Kocagoncu, Anastasia Klimovich-Gray, Laura E. Hughes, and James B. Rowe. Evidence and implications of abnormal predictive coding in dementia. *Brain: A Journal of Neurology*, 144(11):3311–3321, December 2021.

[137] Frank Jessen, Rebecca E. Amariglio, Martin van Boxtel, Monique Breteler, Mathieu Ceccaldi, Gaël Chételat, Bruno Dubois, Carole Dufouil, Kathryn A. Ellis, Wiesje M. van der Flier, Lidia Glodzik, Argonde C. van Harten, Mony J. de Leon, Pauline McHugh, Michelle M. Mielke, Jose Luis Molinuevo, Lisa Mosconi, Ricardo S. Osorio, Audrey Perrotin, Ronald C. Petersen, Laura A. Rabin, Lorena Rami, Barry Reisberg, Dorene M. Rentz, Perminder S. Sachdev, Vincent de la Sayette, Andrew J. Saykin, Philip Scheltens, Melanie B. Shulman, Melissa J. Slavin, Reisa A. Sperling, Robert Stewart, Olga Uspenskaya, Bruno Vellas, Pieter Jelle Visser, Michael Wagner, and Subjective Cognitive Decline Initiative (SCD-I) Working Group. A conceptual framework for research on subjective cognitive decline in preclinical Alzheimer's disease. *Alzheimer's & Dementia: The Journal of the Alzheimer's Association*, 10(6):844–852, November 2014.

[138] F. Passetti and others. Multiple cross-frequency coupling analysis of resting-state EEG in MCI and AD. *Frontiers in Neuroscience*, 17:1149289, 2023.

[139] M. Martinez-Losa and others. Nav1.1-overexpression in mouse prefrontal interneurons reverses cognitive deficits and gamma abnormalities in an Alzheimer's model. *Nature Medicine*, 24(3):358–364, 2018.

[140] Elias P. Casula, Maria C. Pellicciari, Sonia Bonnì, Ilaria Borghi, Michele Maiella, Martina Assogna, Marilena Minei, Caterina Motta, Alessia D'Acunto, Francesco Porrazzini, Valentina Pezzopane, Lucia Mencarelli, Andrea Roncaioli, Lorenzo Rocchi, Danny A. Spampinato, Carlo Caltagirone, Emiliano Santarnecchi, Alessandro Martorana, and Giacomo Koch. Decreased Frontal Gamma Activity in Alzheimer Disease Patients. *Annals of Neurology*, 92(3):464, July 2022.

[141] Karan Govindpani, Beatriz Calvo-Flores Guzmán, Chitra Vinnakota, Henry J. Waldvogel, Richard L. Faull, and Andrea Kwakowsky. Towards a Better Understanding of GABAergic Remodeling in Alzheimer's Disease. *International Journal of Molecular Sciences*, 18(8):1813, August 2017.

[142] Clare E. Palmer, Marco Davare, and James M. Kilner. Physiological and Perceptual Sensory Attenuation Have Different Underlying Neurophysiological Correlates. *The Journal of Neuroscience*, 36(42):10803–10812, October 2016.

[143] Marika Mariano, Ileana Rossetti, Angelo Maravita, Eraldo Paulesu, and Laura Zapparoli. Sensory Attenuation Deficit and Auditory Hallucinations in Schizophrenia: A Causal Mechanism or a Risk Factor? Evidence From Meta-Analyses on the N1 Event-Related Potential Component. *Biological Psychiatry*, 96(3):207–221, August 2024.

[144] Ana Margarida Gonçalves and Patricia Monteiro. Autism Spectrum Disorder and auditory sensory alterations: a systematic review on the integrity of cognitive and neuronal functions related to auditory processing. *Journal of Neural Transmission*, 130(3):325–408, 2023.

[145] Federica Filice, Lucia Janickova, Thomas Henzi, Alessandro Bilella, and Beat Schwaller. The Parvalbumin Hypothesis of Autism Spectrum Disorder. *Frontiers in Cellular Neuroscience*, 14, December 2020. Publisher: Frontiers.

[146] Ewelina Bogdańska-Chomczyk, Maciej Równiak, Andrew Chih-Wei Huang, and Anna Kozłowska. Parvalbumin interneuron deficiency in the prefrontal and motor cortices of spontaneously hypertensive rats: an attention-deficit hyperactivity disorder animal model insight. *Frontiers in Psychiatry*, 15, March 2024. Publisher: Frontiers.

[147] Dadao An, Yi You, Qianyi Ma, Zhengyi Xu, Zonghan Liu, Ruichu Liao, Han Chen, Yiquan Wang, Yi Wang, Haibin Dai, Haohong Li, Lei Jiang, Zhong Chen, and Weiwei Hu. Deficiency of histamine H2 receptors in parvalbumin-positive neurons leads to hyperactivity, impulsivity, and impaired attention. *Neuron*, 113(4):572–589.e6, February 2025.

[148] Beulah Leitch. Parvalbumin Interneuron Dysfunction in Neurological Disorders: Focus on Epilepsy and Alzheimer's Disease. *International Journal of Molecular Sciences*, 25(10):5549, January 2024. Number: 10 Publisher: Multidisciplinary Digital Publishing Institute.

[149] Pablo Juarez and Verónica Martínez Cerdeño. Parvalbumin and parvalbumin chandelier interneurons in autism and other psychiatric disorders. *Frontiers in Psychiatry*, 13, October 2022. Publisher: Frontiers.

[150] Peter F. Liddle and Elizabeth B. Liddle. Imprecise Predictive Coding Is at the Core of Classical Schizophrenia. *Frontiers in Human Neuroscience*, 16, March 2022. Publisher: Frontiers.

[151] Zenas C. Chao, Misako Komatsu, Madoka Matsumoto, Kazuki Iijima, Keiko Nakagaki, and Noritaka Ichinohe. Erroneous predictive coding across brain hierarchies in a non-human primate model of autism spectrum disorder. *Communications Biology*, 7(1):1–16, July 2024. Publisher: Nature Publishing Group.

[152] Maria Luz Gonzalez-Gadea, Srivas Chennu, Tristan A. Bekinschtein, Alexia Rattazzi, Ana Beraudi, Paula Tripicchio, Beatriz Moyano, Yamila Soffita, Laura Steinberg, Federico Adolfi, Mariano Sigman, Julian Marino, Facundo Manes, and Agustin Ibanez. Predictive coding in autism spectrum disorder and attention deficit hyperactivity disorder. *Journal of Neurophysiology*, 114(5):2625–2636, November 2015.

[153] Jorge F. Mejias, John D. Murray, Henry Kennedy, and Xiao-Jing Wang. Feedforward and feedback frequency-dependent interactions in a large-scale laminar network of the primate cortex. *Science Advances*, 2(11):e1601335, 2016.

[154] Mojtaba Chehelcheraghi, Chie Nakatani, Erik Steur, and Cees van Leeuwen. A neural mass model of phase–amplitude coupling. *Biological Cybernetics*, 110(2-3):171–192, 2016.

[155] Roberto C. Sotero. Topology, cross-frequency, and same-frequency band interactions shape the generation of phase-amplitude coupling in a neural mass model of a cortical column. *PLOS Computational Biology*, 12(11):e1005180, 2016.

[156] Andrea Ceni, Simona Olmi, Alessandro Torcini, and David Angulo-Garcia. Cross frequency coupling in next generation inhibitory neural mass models. *Chaos*, 30(5):053121, 2020.

[157] Marco Segneri, Hongjie Bi, Simona Olmi, and Alessandro Torcini. Theta-nested gamma oscillations in next generation neural mass models. *Frontiers in Computational Neuroscience*, 14:47, 2020.

[158] Adam Ponzi, Salvador Dura-Bernal, and Michele Migliore. Theta-gamma phase amplitude coupling in a hippocampal ca1 microcircuit. *PLoS Computational Biology*, 19(3):e1010942, 2023.

[159] Nikola Jajcay, Caglar Cakan, and Klaus Obermayer. Cross-frequency slow oscillation–spindle coupling in a biophysically realistic thalamocortical neural mass model. *Frontiers in Computational Neuroscience*, 16:769860, 2022.

[160] Michael W. Spratling. Reconciling predictive coding and biased competition models of cortical function. *Frontiers in Computational Neuroscience*, 2:4, 2008.

[161] Catherine Wacongne, Jean-Pierre Changeux, and Stanislas Dehaene. A neuronal model of predictive coding accounting for the mismatch negativity. *Journal of Neuroscience*, 32(11):3665–3678, 2012.

[162] Andr
'e M. Bastos, W. Martin Usrey, Rick A. Adams, G. R. Mangun, Pascal Fries, and Karl J. Friston. Canonical microcircuits for predictive coding. *Neuron*, 76(4):695–711, 2012.

[163] Yuru Song, Mingchen Yao, Helen Kemprecos,
'Aine Byrne, Zhengdong Xiao, Qiaosheng Zhang, Amrita Singh, Jing Wang, and Zhe S. Chen. Predictive coding models for pain perception. *Journal of Computational Neuroscience*, 49(2):107–127, 2021.

[164] H. F. Iaccarino and others. Gamma frequency entrainment attenuates amyloid load and modifies microglia in an Alzheimer's disease model. *Nature*, 540(7632):230–235, 2016.

A Band power and PEIX plots

The following plots illustrate how power distributions within each frequency band are influenced by the mean external inputs to the respective populations.

We also display PEIX, a normalized slope measure of excitation–inhibition balance. Neural populations are often modeled by a sigmoid function,

$$S(V) = \frac{2e_0}{1 + \exp\big(r(V_0 - V)\big)},$$

where V_0 is the half-maximum potential (the linear operating point), e_0 is the maximum firing rate, and r sets the slope. The derivative,

$$S'(V) = \frac{2e_0\, r\, \exp\big(r(V_0 - V)\big)}{\Big(1 + \exp\big(r(V_0 - V)\big)\Big)^2},$$

peaks at $V = V_0$ with $S'(V_0) = \frac{e_0 r}{2}$ and decreases as the system enters its excitatory ($V \gg V_0$) or inhibitory ($V \ll V_0$) saturation regimes.

To quantify the deviation from the ideal linear regime, we define the dimensionless variable

$$x = r\big(\langle V \rangle - V_0\big),$$

where $\langle V \rangle$ is the average membrane potential. By normalizing the local slope $S'(V)$ with its maximum value at V_0, we obtain a measure of nonlinearity that distinguishes between excitation and inhibition. The **Population Excitation-Inhibition Index (PEIX)** is defined as

$$\mathcal{X}\,(x) = -\operatorname{sign}(x)\left(\frac{4\,\exp(-x)}{\Big(1 + \exp(-x)\Big)^2} - 1\right).$$

This formulation ensures that:

- $\mathcal{X}\,(x) \approx 0$ when $\langle V \rangle \approx V_0$ (linear regime),
- $\mathcal{X}\,(x) > 0$ when $\langle V \rangle > V_0$ (excitatory state),
- $\mathcal{X}\,(x) < 0$ when $\langle V \rangle < V_0$ (inhibitory state),
- $|\,\mathcal{X}\,(x)| \approx 1$ in the saturated regimes.

Thus, by focusing on the normalized slope of the sigmoid, PEIX provides a compact, dimensionless index of both the deviation from the optimal operating point and the underlying excitation–inhibition balance.

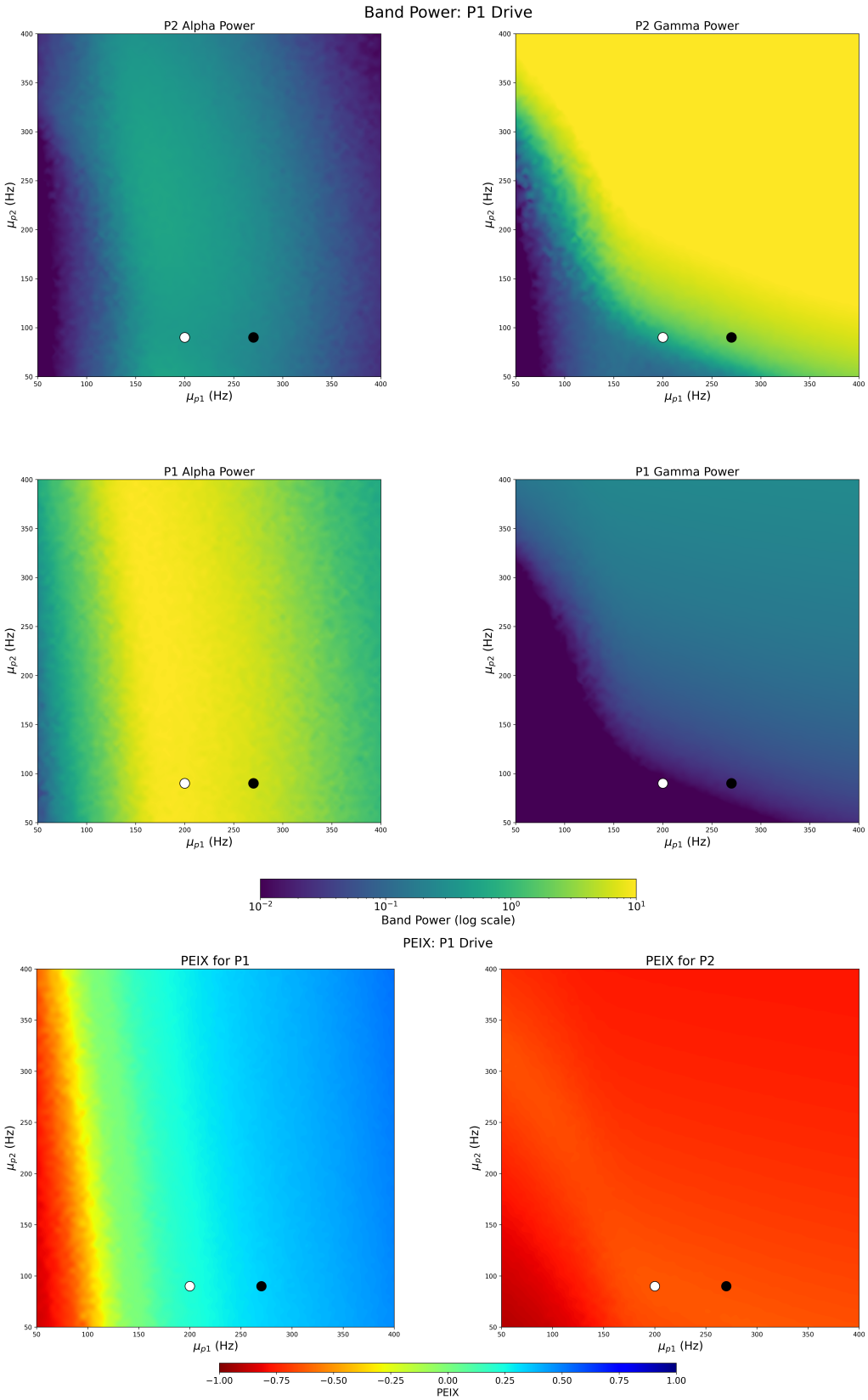

Figure A1: LaNMM band power for P_1 and P_2 populations for varying external mean drives μ_{P_1} and μ_{P_2} (stochastic drive on P_1). The left column displays the alpha band power $(8-12\,\text{Hz})$ for P_1 and P_2, while the right column shows the gamma band power $(30-50\,\text{Hz})$ for each population. The white dot marks the mean input parameter values used in Sanchez-Todo el al. (2023),[86] $(\mu_{P_1}, \mu_{P_2}) = (200, 90)$ Hz. The black dot indicates the values chosen for this study, $(\mu_{P_1}, \mu_{P_2}) = (270, 90)$ Hz. The bottom plot displays the PEIX indicator.

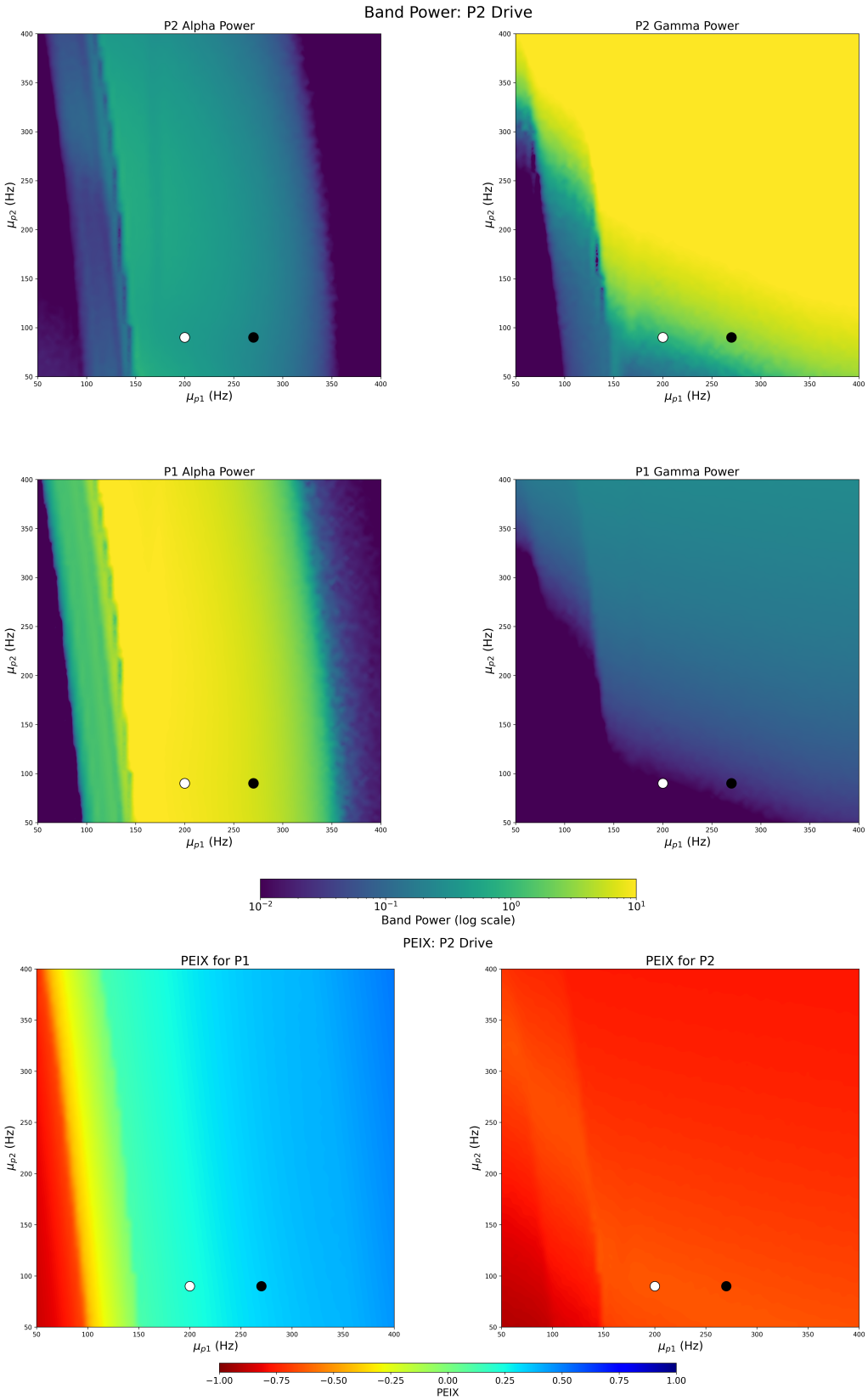

Figure A2: LaNMM band power for P_1 and P_2 populations for varying external mean drives μ_{P_1} and μ_{P_2} (stochastic drive on P_2). The left column displays the alpha band power $(8-12\,\text{Hz})$ for P_1 and P_2, while the right column shows the gamma band power $(30-50\,\text{Hz})$ for each population. The white dot marks the mean input parameter values used in Sanchez-Todo et al. (2023),[86] $(\mu_{P_1}, \mu_{P_2}) = (200, 90)$ Hz. The black dot indicates the values chosen for this study, $(\mu_{P_1}, \mu_{P_2}) = (270, 90)$ Hz, which is deeper into the quasi periodic regime with stronger EEC (see Figures 4 and H1. The bottom plot displays the PEIX indicator.

B Gain optimization

In this section, we detail the methodology used to select the gains applied to the input and prior messages provided to the LaNMM for the SEC and EEC error computation.

In each case (SEC / EEC), we first selected the input gain $G_{\mathcal{I}}$ so that when the input message was applied alone (no prior), the output of the LaNMM ($\mathcal{E}$) showed a high PCC with the input message. This way, we could ensure that the input was strong enough to modulate the activity of the LaNMM and carry it through the output message. As shown in Figure B1, if the input gain is sufficiently high, the output is highly correlated with the input. However, the higher the input gain, the more it would dominate the output message and the harder it would be to suppress it with a prior message. We thus selected in each case the lowest input gain that resulted in high PCC with the input, i.e., $G^*_{\mathcal{I}}(SEC) = 10$ and $G^*_{\mathcal{I}}(EEC) = 1$.

For the SEC mechanisms, we used the selected input gain and evaluated the $\mathcal{E}$ power as a function of the prior gain in the case when a prior message matching the input was sent to the LaNMM. We studied the cases where the prior was sent to the P1 population and to the PV population. In each case, there was an optimal value of prior gain that would lead to a minimum error, as shown in Figure B1. We chose the nearest round values that better approximated such a minimum, i.e., $G^*_{\mathcal{P}}(SEC, P1) = 20$, $G^*_{\mathcal{P}}(SEC, PV) = 5$.

For the EEC mechanism, we used the selected input gain and evaluated for different prior gains the MSE between the subtraction of input precision and prior precision and the error precision, as shown in Figure 10. We selected the nearest round value of prior gain that resulted in the minimum MSE, $G^*_{\mathcal{P}}(EEC) = 10$.

C Input-prior phase dependence (SEC)

We expected that for effective suppression of the input signal with a matching prior using the SEC mechanism the prior signal sent to P1 had to be phase-shifted by 180º (i.e., inverted). This inversion would allow the prediction message to counteract the excitatory input effectively. This was due to the fact that P1 is an excitatory population and that the SEC for P1-driving inputs is positive, as shown in Figure 4. We confirmed this by computing the power of the output from the LaNMM $\mathcal{E}$ when varying the phase of the matching prior (see Figure C1a). Interestingly, we can see that when applying the matching prior in phase with the input (0º shift), the output error is increased with respect to the flat prior and wrong prior conditions.

In contrast, for the PV population, which is inhibitory and has positive SEC for PV-driving inputs, the prior had to be applied in phase with the input signal to achieve suppression (see Figure C1b. When priors shifted 180º (inverted) where sent to the PV population, the LaNMM output $\mathcal{E}$ power was increased.

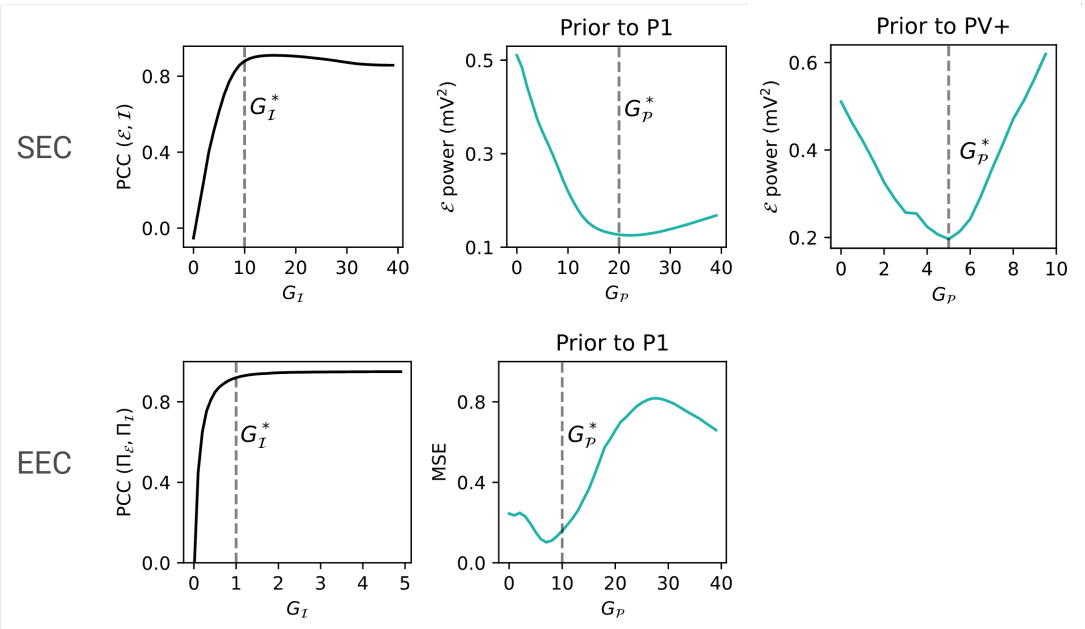

Figure B1: Selection of input and prior gains for SEC and EEC. Top and bottom panels show the gain optimization process for SEC and EEC, respectively. Left panels: Pearson correlation coefficient (PCC) between the LaNMM error signal $\mathcal{E}$ and the input message $\mathcal{I}$ as a function of input gain $G_\mathcal{I}$. The selected gain $G_\mathcal{I}^*$ (dashed line) corresponds to the lowest value that ensures a high PCC. Middle and right panels: $\mathcal{E}$ power (top) and MSE (bottom) as a function of prior gain $G_\mathcal{P}$, showing a clear minimum when the prior matches the input. The selected prior gain $G_\mathcal{P}^*$ (dashed line) approximates the value that minimizes error power.

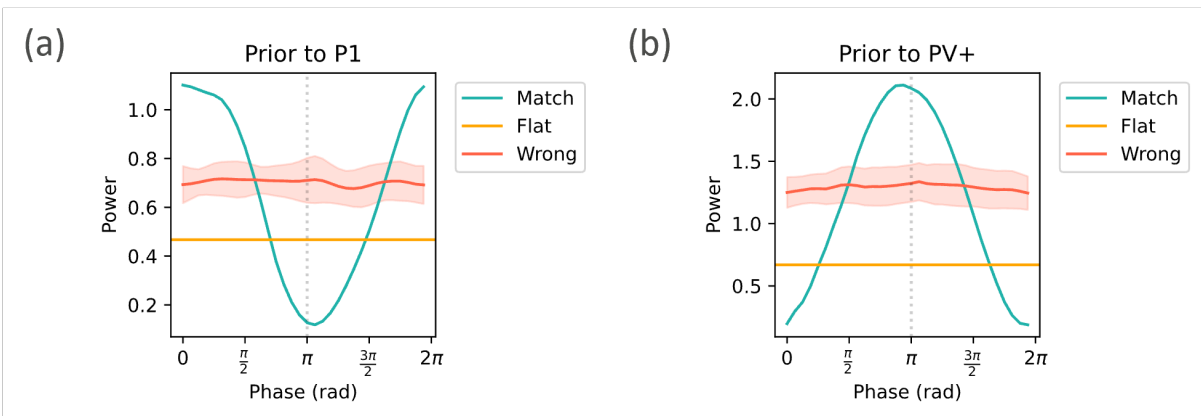

Figure C1: $\mathcal{E}$ power as a function of the phase shift of the prior with respect to the input signal. Different prior configurations are used: matching prior ("match"), wrong prior ("other") and flat prior ("base"). (a) Prior to P1 condition. (b) Prior to PV condition.

D Precision and Kalman Gain

In the Kalman filtering framework, updating the state estimate involves balancing prior predictions with incoming measurements. At step k, this balance is quantified by the innovation covariance S_k, defined as:

$$S_k = HP_k^- H^T + R, \tag{6}$$

where:

- P_k^- is the predicted (prior) state covariance, reflecting the uncertainty inherent in the internal model's prediction of the current state before incorporating new observations.
- H is the observation model, projecting uncertainty from state-space into measurement-space, transforming prior state uncertainty P_k^- into observation uncertainty $HP_k^- H^T$.
- R is the measurement noise covariance, explicitly encoding uncertainty or noise inherent to the measurements themselves, independent of the model.

Thus, the innovation covariance S_k combines two distinct sources of uncertainty:

1. **Model-based uncertainty ($HP_k^- H^T$):** uncertainty arising from the prediction step, reflecting imprecision in the model's prior expectation about the observed quantities.
2. **Measurement uncertainty (R):** intrinsic uncertainty in the data, reflecting how noisy or unreliable the incoming observations are.

The precision matrix Π_k, defined as the inverse of S_k, explicitly integrates both these uncertainties:

$$\Pi_k = S_k^{-1} = \left(HP_k^- H^T + R\right)^{-1}. \tag{7}$$

Higher precision thus means lower combined uncertainty, increasing confidence in the prediction errors.

The Kalman gain K_k, directly related to precision, weights prediction errors (innovations) when updating the state estimate:

$$K_k = P_k^- H^T \Pi_k. \tag{8}$$

Finally, the posterior state estimate $\hat{x}_k^+$ is updated using this gain applied to the prediction error $\nu_k = z_k - H\hat{x}_k^-$:

$$\hat{x}_k^+ = \hat{x}_k^- + K_k \nu_k. \tag{9}$$

Precision thus clearly separates and balances model-derived and measurement-derived uncertainties, directly controlling the integration of observational evidence into state inference.

E Predictive Routing from EEC

In predictive routing,[21] *information is encoded by route* and predictions address the route taken by sensory stimuli: correctly predicted inputs are inhibited, while unpredicted inputs propagate,

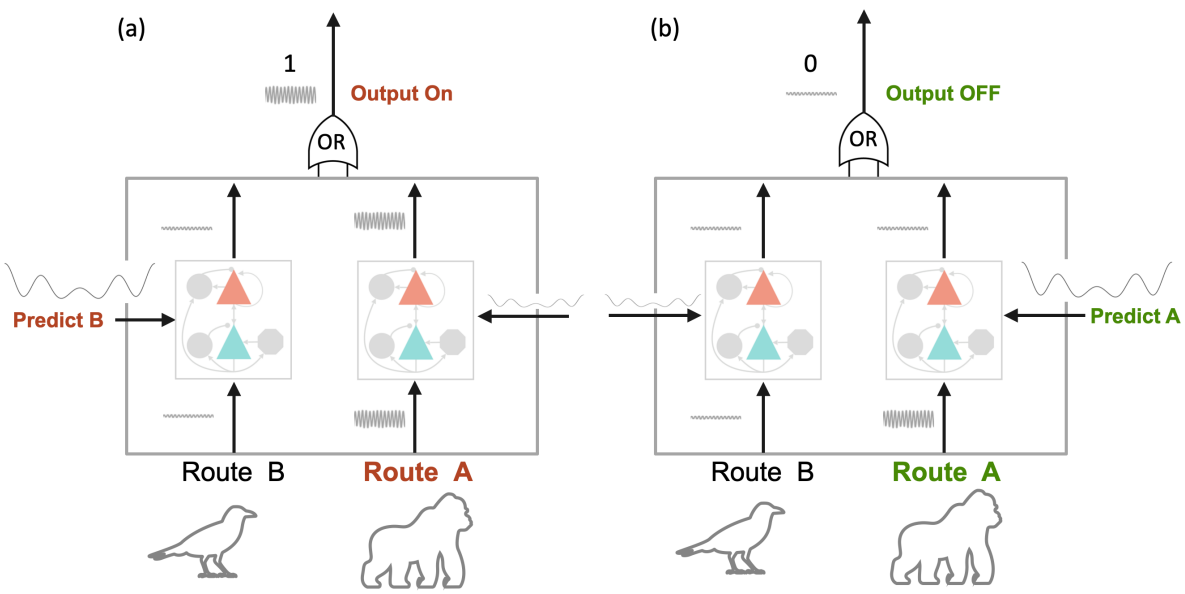

Figure E1: Predictive routing: prediction of the route of the stimulus: *information = route*. Bottom-up stimulus travels via route A or B (encoding 0 or 1, respectively), depending on the stimulus. In the depicted case, it travels via Route A (encoding a 1). The prediction aims to predict the route and inhibit information flow. Inhibition is implemented via EEC or SEC. (a) The route is incorrectly predicted (prediction on the left, encoding a 0), so the signal flows through (XOR(0,1)=1 on top, Output is ON). (b) The route is correctly predicted (Route 1 is predicted), and information flow is suppressed (XOR(0,0)=0).

signaling prediction errors.

Top-down predictions are communicated via alpha/beta oscillations (8–30 Hz) originating from deep cortical layers. These rhythms prepare sensory pathways by pre-emptively inhibiting the columns that process expected inputs. It is this pre-emptive aspect that reflects predictions of which prediction errors will convey precise or salient information.

When a prediction specifies a particular route—say, Route A—the corresponding cortical column is suppressed by alpha/beta activity, which in turn reduces gamma oscillations and neuronal spiking in that column. As a consequence, expected stimuli arriving via Route A are effectively blocked. Conversely, when the prediction is off (inhibition of Route B), the stimulus bypasses the inhibitory control because the predicted pathway is not engaged, generating an active output. In this case, the absence of alpha/beta-mediated inhibition allows for enhanced gamma oscillations and increased spiking activity, which serve as a robust signal of a prediction error. Figure E1 illustrates this process: when predictions indicate that a stimulus will follow Route A, alpha/beta rhythms suppress gamma activity in the corresponding cortical column, blocking that pathway. If the actual input follows Route B, the lack of inhibition permits gamma activity and spiking, thereby signaling a prediction error and routing unpredicted information upward in the cortical hierarchy. This provides a distributed implementation of the Comparator using multiple columns.

F LaNMM examples in other bands

Here we provide a couple of examples of the spectra produced by other parameter configurations in LaNMM, obtained by changing synaptic time constants.

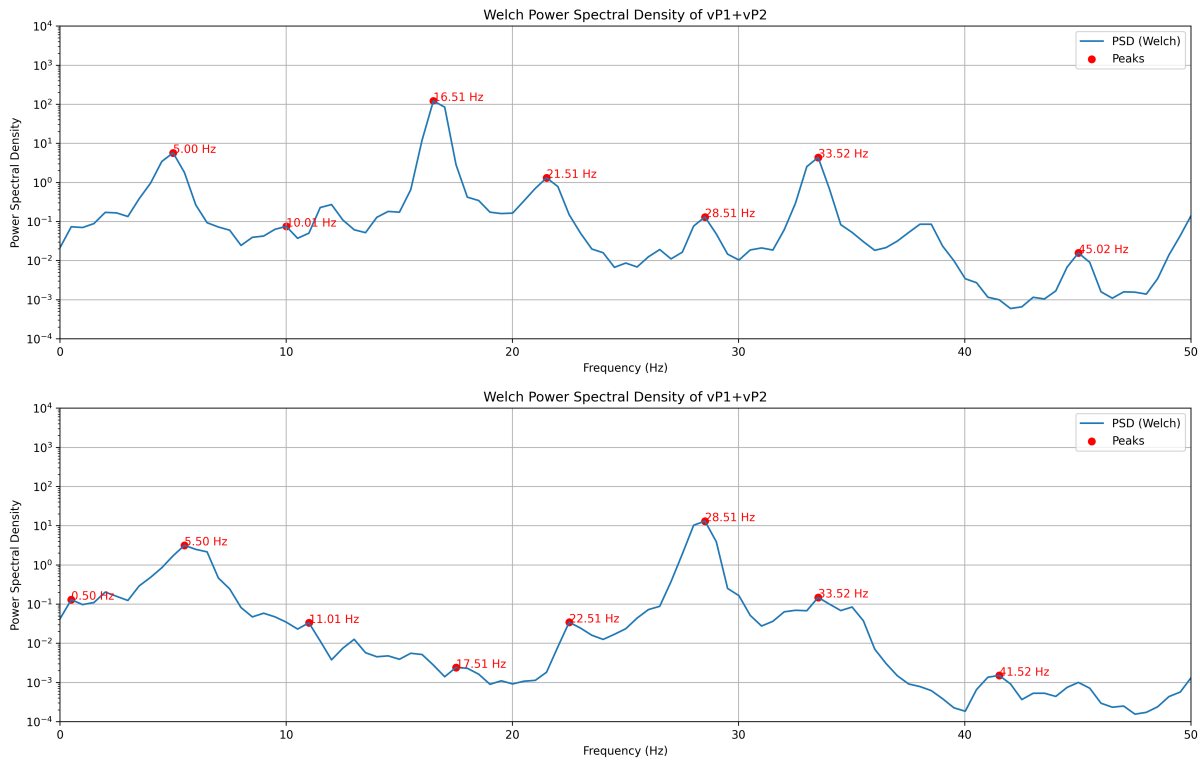

Figure F1: Examples from other LaNMM parameter configurations (only changing time constants).

G Noise generation for SEC and EEC characterization

The external driving inputs to P_1 and P_2 used in Figure 4 were crafted using a multiscale noise generator that amalgamates slow and fast fluctuations. The noise was generated by combining two components: a slow drift and a fast fluctuation. The slow drift was produced using an autoregressive (AR(1)) process with coefficient α_{slow}, yielding an effective timescale $\tau_{\text{slow}} = -\Delta t/\ln(\alpha_{\text{slow}})$, which captures long-term fluctuations. The fast component was generated as white noise, scaled by a standard deviation σ_{fast}, and then low-pass filtered with a 4th-order Butterworth filter having a cutoff frequency f_{cutoff}, resulting in an effective timescale $\tau_{\text{fast}} = 1/(2\pi f_{\text{cutoff}})$. These two components were summed and offset by a base mean, and values were clipped to a minimum floor to prevent extremely small or negative outputs. Noise was generated over the simulation time vector with a sampling frequency $f_s = 1/\Delta t$, and reproducibility was ensured by setting a fixed random seed.

Figure G1 shows an example of the multiscale noise generated and its power spectral density.

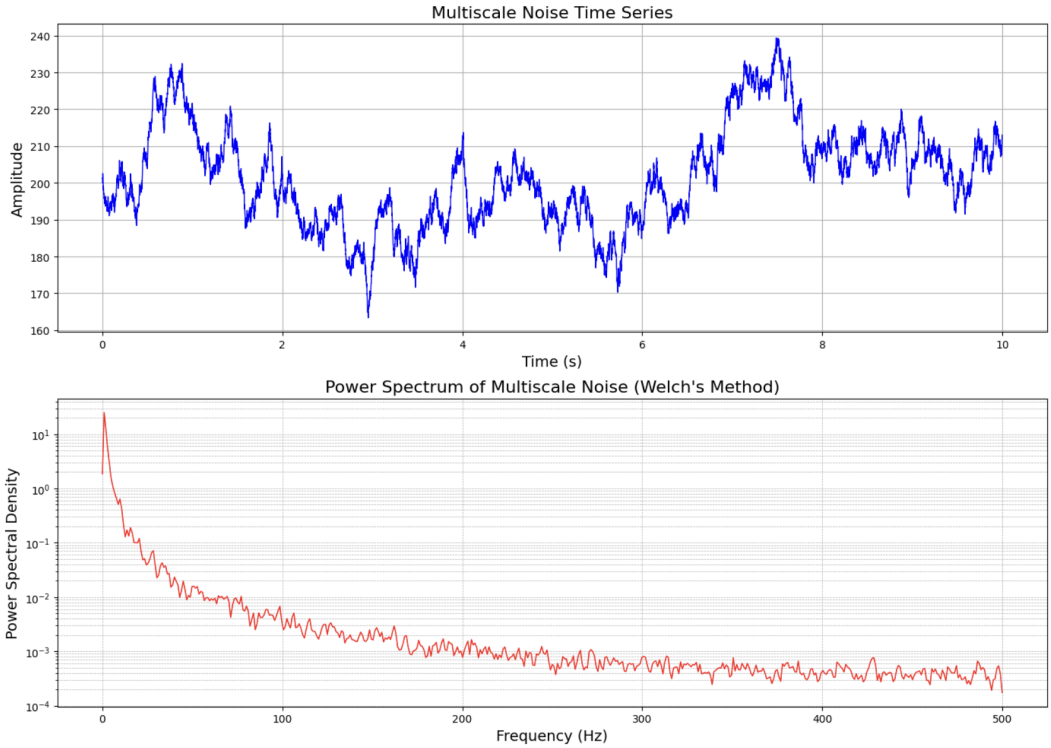

Figure G1: Example of multiscale noise (top panel) and its power spectral density (bottom panel).

H SEC and EEC under AM modulation driving

Generation of AM-Modulated Signals. To evaluate the impact of AM driving vs noise, we generated amplitude-modulated (AM) signals in the alpha band by applying nested modulation to a carrier tone.[100] Formally, given a time array t, a carrier frequency f_c, and two bandpass filters for modulators $m_1(t)$ and $m_2(t)$, we compute

$$S(t) \;=\; E(t)\,\cos(2\pi f_c\,t),$$

where the envelope $E(t)$ is defined as

$$E(t) \;=\; A_c\,\big[1 + a_1\,m_1(t)\big]\,\big[1 + a_2\,m_2(t)\big].$$

where a_1 and a_2 are the modulation indexes. In practice, $m_1(t)$ and $m_2(t)$ are obtained by bandpass filtering white noise within the specified frequency bands (*envelope_band* and *slow_band*, respectively), and the filtered signals are then rescaled to the range $[-1, 1]$. The final AM-modulated signal $S(t)$ is shifted to have zero mean. This nested structure allows the fast modulator to impose rapid changes in amplitude on the carrier, while the slow modulator introduces additional variations over longer timescales. In our simulation of priors, we set $f_c = 0$, as we are interested in the modulated envelope only.

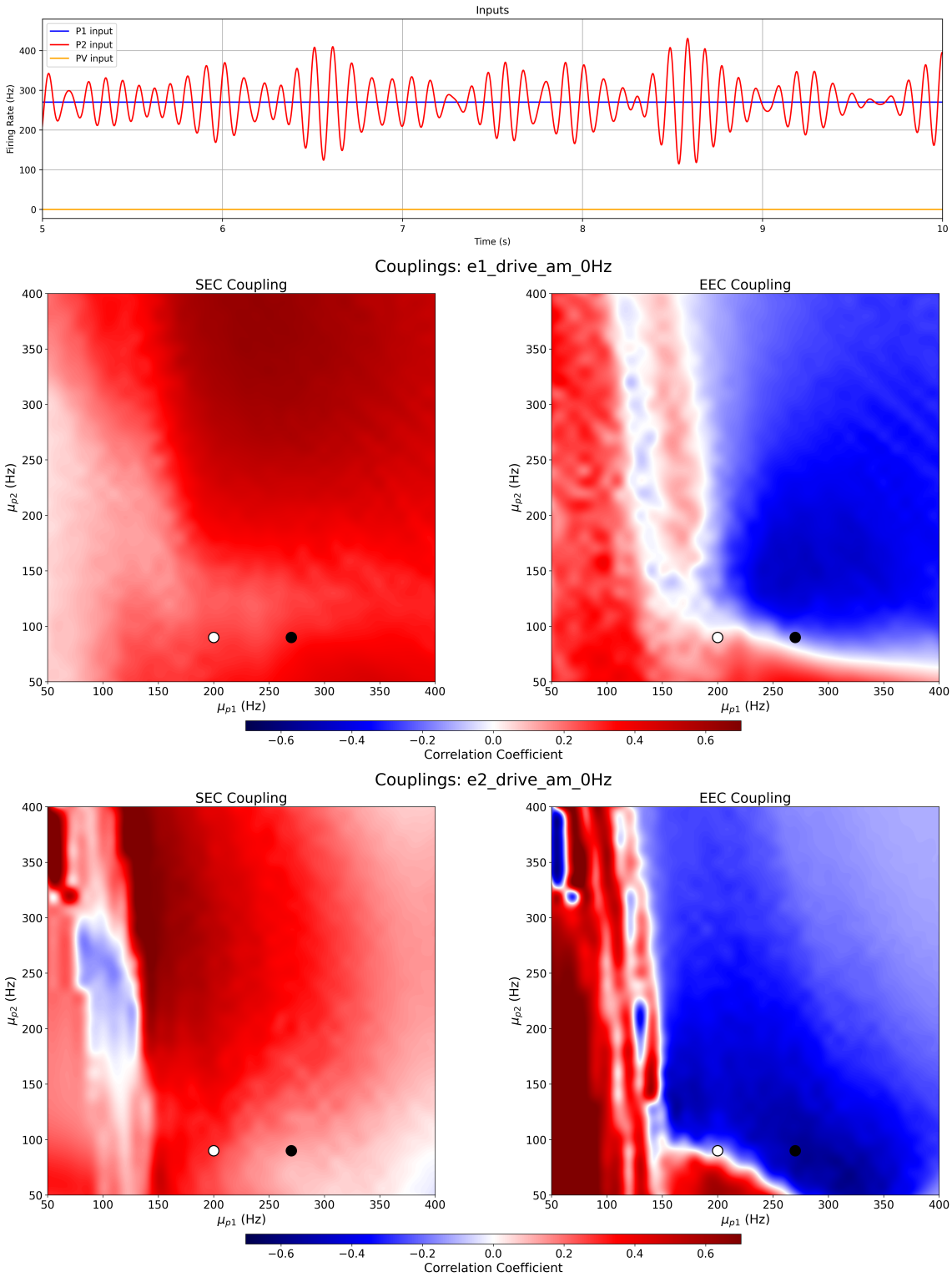

Figure H1: Top: sample modulation signal. Bottom: Couplings for P1 and P2 driving under AM modulation. Modulation used a 0.5-2 Hz modulation of a 8-12 Hz band signal.